ACS APPLIED MATERIALS & INTERFACES

www.acsami.org Research Article

Suppression of Filament Defects in Embedded 3D Printing

Leanne M. Friedrich,* Ross T. Gunther, and Jonathan E. Seppala

Cite This: https://doi.org/10.1021/acsami.2c08047 Read Online

ABSTRACT: Embedded 3D printing enables the manufacture of soft, intricate structures. In the technique, a nozzle is embedded into a viscoelastic support bath and extrudes filaments or droplets. While embedded 3D printing expands the printable materials space to low-viscosity fluids, it also presents new challenges. Filament cross-sections can be tall and narrow, have sharp edges, and have rough surfaces. Filaments can also rupture or contract due to capillarity, harming print fidelity. Through digital image analysis of in situ videos of the printing process and images of filaments just after printing, we probe the effects of ink and support rheology, print speeds, and interfacial tension on defects in individual filaments. Using model materials, we determine that if both the ink and support are water-based, the local viscosity ratio near the nozzle controls the filament shape. If the ink is slightly more viscous than the support, a round, smooth filament is produced. If the ink is oil-based and the support is water-based, the capillary number, or the product of the ink speed and support viscosity divided by the interfacial tension, controls the filament shape. To suppress contraction and rupture, the capillary number should be high, even though this leads to trade-offs in roughness and roundness. Still, inks at nonzero interfacial tension can be advantageous, since they lead to much rounder and smoother filaments than inks at zero interfacial tension with equivalent viscosity ratios.

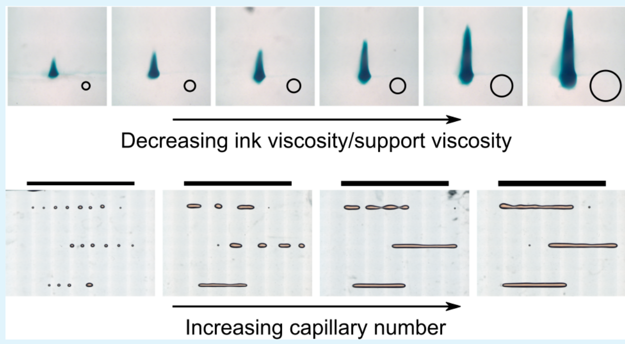

KEYWORDS: *3D printing, extrusion, support bath, Herschel−Bulkley, rheology, surface tension*

■ INTRODUCTION

The proliferation of 3D-printing techniques has enabled the fabrication of complex, custom structures in a wide range of materials. Each printing technique is limited to a particular materials space. For example, inkjet printing is well-suited to low-viscosity photopolymers, while fused deposition modeling is restricted to thermoplastics.[1] Direct ink writing (DIW), wherein continuous filaments are extruded onto a substrate and subsequently cured, requires extrudable and self-supporting viscoelastic materials.[1] Recently, embedded 3D printing has enabled the fabrication of soft, low-viscosity materials and is particularly useful for bioprinting.[2−4] In embedded 3D printing, a nozzle is submerged into a support bath, which is usually a viscoelastic gel. The nozzle either extrudes continuous filaments, for embedded ink writing (EIW), or droplets, for embedded droplet printing (EDP),[5] into the support bath. The printed part can be cured via light, pH, thermal curing, or introduction of a cross-linker such as an enzyme or ion and then extracted via rinsing, melting, or dissolution of the print bath.[4] Alternatively, the support can be cured and the ink can be removed,[6] or both can be cured.[7] Because the bath holds the form of the printed part, embedded 3D printing expands the materials space to include lower-viscosity materials, expands the toolpath space to include vertical lines instead of being constrained to $x-y$ layers, and expands the design space to include fine structures and embedded multiphase components.[8] Embedded 3D printing is known by many aliases, including “freeform 3D printing”,[9−12] “freeform reversible embedding (FRE)”,[4,13−15] “guest−host writing (GHost writing)”,[16] “sacrificial writing into functional tissue (SWIFT)”,[17] “suspended layer additive manufacturing (SLAM)”,[18,19] and “writing in granular gels”.[8,20] Notably, EIW allows incorporation of cells into bio-inks, which can improve cell adhesion compared to seeding cells on printed scaffolds.[12,13,21−24]

While it presents new opportunities, embedded 3D printing presents unique challenges in print quality. Whereas filaments in DIW and fused deposition modeling tend to be short and wide as they spread and are squeezed between the nozzle and the substrate,[25,26] EIW filaments tend to be tall and narrow.[18,27−29] If filament−filament interfaces are weaker or less conductive or have lower cell concentrations than the centers of the filaments, large filament aspect ratios could lead to anisotropy in the full part. Some EIW filaments have sharp edges and triangular cross-sections,[10,23,27,30] while others have

Received: May 6, 2022
Accepted: June 20, 2022

Table 1. Variables Referenced in This Work for Ink and Support

d_i, d_o	inner, outer nozzle diameters	
d_{est}	programmed filament diameter	$d_i\sqrt{v_{ink}/v_{sup}}$
v_{ink}	ink velocity	ink flux/nozzle area
v_{sup}	support velocity	stage translation speed
$\dot{\gamma}_{ink}$, $\dot{\gamma}_{sup}$	shear rates	
η_{ink}, η_{sup}	local viscosities	
ρ_{ink}, ρ_{sup}	densities	
σ	interfacial tension	
$\tau_{y,ink}$, $\tau_{y,\,sup}$	shear yield stresses	
Bm_{ink}, Bm_{sup}	Bingham number	yield stress/viscous dissipation
Ca_{ink}, Ca_{sup}, Ca	capillary number	viscous dissipation/interfacial tension
$\overline{d_{PR,ink}}$, $\overline{d_{PR,sup}}$	normalized critical diameter	yield stress/interfacial tension
Oh_{ink}, Oh_{sup}	Ohnesorge number	viscous dissipation/($\sqrt{\text{inertia} \times \text{interfacial tension}}$)
Re_{ink}, Re_{sup}	Reynolds number	inertia/viscous dissipation
We_{ink}, We_{sup}	Weber number	inertia/interfacial tension

round cross-sections.[27,30] In addition to sharp edges, some material systems produce filaments with rough surfaces.[13,14,31−33] Filament surface roughness and sharp edges could introduce porosity to the final part,[13] trap support material,[13] or introduce surface roughness to the final part and inhibit removal from the bath.[7] This work uses parameter sweeps to directly probe the effect of interfacial tension, ink and support rheology, and printing speeds on cross-sectional shape and surface roughness. Critically, we find that rounder, smoother filaments are produced as the local ink viscosity to support viscosity ratio increases and the capillary number decreases.

Although filaments can rupture in DIW,[34] the lack of substrate pinning introduces new rupture modes in EIW, including Plateau−Rayleigh instabilities[2] and cell-induced rupture and buckling.[35] These rupture modes can be leveraged for EDP, but control of droplet size and frequency is critical.[5] Multiple theories have been proposed that connect 24 h filament stability to the ratio between the interfacial tension and mechanical and rheological properties of the filament including the ink elastic modulus, support shear yield stress, and ink tensile yield stress.[5,32,36] However, these previous relationships describe long-term behaviors of inks and supports that have recovered, so the critical energetic contributions are elastic. In many embedded 3D-printing applications, the filaments are cured soon after printing, via interaction with a cross-linker in the bath, exposure to a curing light, or pH change upon interaction with the bath.[4] In these scenarios, the short-term behavior of the filament is critical, so the viscous behavior of the filament and bath may be more important than the elastic behavior. In this work, we sweep through inks and supports of varying rheological modifier concentrations, known interfacial tensions, and print speeds. These results show that, in the short term, the capillary behaviors of printed filaments correlate just as strongly with local viscosity-based scaling factors as yield stress-based scaling factors. Additionally, unlike long time scales, at short time scales there is no critical radius at which filaments break into droplets.

■ SCALING RELATIONSHIPS

Several scaling relationships have been proposed as key tools for controlling print quality in embedded 3D printing. Here, we discuss a few relationships which reflect the relationships between interfacial energy, viscous dissipation, yielding, and inertia in this printing process. In this work, "ratio" refers to the ink value divided by the support value. For example, the viscosity ratio is η_{ink}/η_{sup}. Where velocities are referenced, ink flow speeds are defined as the volume flux of ink divided by the inner cross-sectional area of the nozzle. Support speeds are defined as the translation speed of the stage.

At zero interfacial tension, various rheological and inertial effects could be at play. Simulations of embedded 3D printing which varied the viscosities of the ink and support indicated that the local viscosity ratio, η_{ink}/η_{sup} (Table 1), controls the cross-sectional shape at zero interfacial tension.[29] The viscosity ratio has also been shown to correlate with morphologies of injected and embedded viscous filaments.[37,38] Alternatively, one could consider the Bingham numbers of the ink and support $Bm = \tau_y d/(\eta v)$, where τ_y is the shear yield stress, d is nozzle diameter, η is viscosity, and v is velocity. The Bingham numbers describe the relationship between shear yield stress and viscous dissipation. The support Bingham number, which is similar to the Oldroyd number, has been shown to correlate with flow behaviors during embedded 3D printing and flow of viscoelastic fluids around cylinders.[39−42] Finally, one could consider the Reynolds numbers of the ink and support $Re = \rho v d/\eta$, where ρ is density, which describes the ratio between inertia and viscous dissipation and has also been shown to correlate with flow behavior around a cylinder.[39−41]

At nonzero interfacial tension, there are several ways to balance interfacial tension, σ, against inertia and rheology. The ratio between the interfacial tension and viscosity has been found to correlate with shrinking and rupture in injected filaments.[37] This ratio is contained in the capillary number, Ca, which describes the relationship between viscous dissipation and interfacial tension. The capillary number can be defined separately on each side of the ink−support interface, where $Ca_{ink} = \eta_{ink}v_{ink}/\sigma$ and $Ca_{sup} = \eta_{sup}v_{sup}/\sigma$. Alternatively, the capillary number can be used to describe how viscous dissipation in the support interacts with the flow of ink.

$$Ca = \eta_{sup}v_{ink}/\sigma \tag{1}$$

In embedded 3D printing, the stability of written filaments has been proposed to depend on the critical diameter for Plateau−Rayleigh instabilities, $d_{PR} = \sigma/\tau_{y,sup}$, where a filament with a diameter smaller than d_{PR} will rupture.[2,32] To put the critical diameter in context, we can use the programmed filament diameter $d_{est} = d_i\sqrt{v_{ink}/v_{sup}}$. The critical diameter

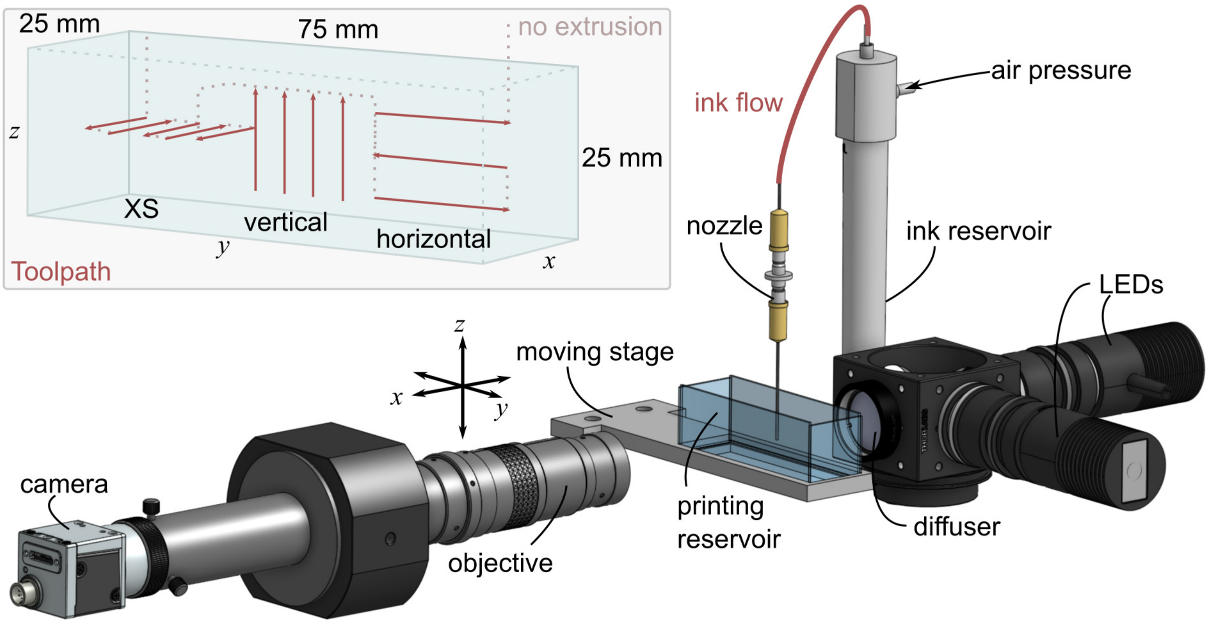

Figure 1. Diagram of printing setup. Inset: Schematic of toolpath. The ink pressure is on for thick lines and off for dotted lines. Arrows indicate writing direction. Models are via refs 49−51.

ratio, $\overline{d_{PR}} = d_{est}/d_{PR}$, describes the likelihood of Plateau−Rayleigh instabilities, where a value greater than 1 indicates that instabilities should be suppressed. Alternatively, the Weber number, $We = \rho v d/\sigma$, which describes the relationship between inertia and interfacial tension, has been shown to correlate with the morphology type in injected filaments.[43] Finally, the Ohnesorge number, $Oh = \eta/\sqrt{\rho d \sigma}$, which describes the relationship between viscous dissipation, inertia, and interfacial tension, is a strong indicator of dripping modes in inkjet printing.[44]

METHODS AND MATERIALS

The data produced for this work, including density measurements, surface tension measurements, flow rate calibration measurements, rheology measurements, Shopbot movement files (equivalent to G-code), videos of the printing process, raw and stitched images of printed structures, time−pressure tables, and extracted metric tables, are available at ref 45. The code used to analyze the data is available at ref 46.

Materials. In all steps in this section where fluids were mixed in a planetary mixer, they were mixed in a Flacktek planetary mixer at 2500 rpm (262 rad/s) for 3 min. Where a mass fraction is cited, it refers to only the mass fraction at the current step, not for the final material. Herein, only mass fractions are used, and "%" refers to the number 0.01.[47] As such, "a mass fraction of 2 % X" refers to 2 g of X out of every 100 g of mixture.

Support gels consisted of Millipore water, Laponite RD (BYK), and, in some cases, Tween 80 (Sigma-Aldrich). Gels were mixed in an overhead stirrer at 400 rpm (4.19 rad/s) for 4 min, where a mass fraction of 2.25−4% of Laponite powder was added slowly to water during stirring. For gels without Tween, gels were poured directly into the printing reservoir and rested for 1 day before printing. For gels with Tween, the Laponite gel rested for 1 day, and then a mass fraction of 0.5% Tween 80 was added to the gel and mixed in a planetary mixer. A 40 g amount of support gel was then poured directly into the 49 mL printing reservoir and rested for 1 day before printing.

Several inks were tested. To create blue water, a mass fraction of 0.01% Nile Blue A dye (Sigma-Aldrich) was added to Millipore water, mixed in a planetary mixer, and rested for at least 1 day. Laponite-based inks were prepared using the same procedure as that for the support gels, but with blue water. Laponite-based inks were printed the day after mixing. For poly(ethylene glycol) diacrylate (PEGDA) inks, a mass fraction of 40% poly(ethylene glycol) diacrylate (number-average molecular mass, M_n 700; Sigma-Aldrich) was added to blue water and mixed in the planetary mixer. A mass fraction of 5−12.5% Aerosil 200 fumed silica (Evonik) was added to the PEGDA/water mixture and mixed in the planetary mixer. PEGDA inks were printed the same day that they were mixed. For mineral oil-based inks, a mass fraction of 0.01% Sudan III red dye (Sigma-Aldrich) was added to white, light mineral oil (Sigma-Aldrich) and mixed in the planetary mixer. Then, a mass fraction of 4−9% Aerosil R812S fumed silica was added to the mineral oil and mixed in the planetary mixer. For mineral oil (MO) inks with surfactant, a mass fraction of 0.5% Span 20 (Sigma-Aldrich) was added to mineral oil and mixed in a planetary mixer before adding fumed silica. Mineral oil and mineral oil/Span inks were printed the day after mixing. For poly(dimethylsiloxane) (PDMS) inks, vinyl-terminated poly(dimethylsiloxane) (molecular mass, 28 000 g/mol; 1000 cSt; Gelest DMS-V31) was combined with [2−3% (mercaptopropyl)methylsiloxane] − dimethylsiloxane copolymer (molecular mass, 6000−8000 g/mol; 120−180 cSt; Gelest SMS-022) at a 3:1 mass ratio and mixed in the planetary mixer. A mass fraction of 0.05% Sudan III red dye was added to the PDMS mixture and mixed in the planetary mixer. A mass fraction of 5% to 12.5% Aerosil R812S fumed silica was added to the PDMS mixture and mixed in a planetary mixer. Finally, a mass fraction of 25% mineral oil or silicone oil (SO) (20 cSt; Sigma-Aldrich) was added to the mixture and mixed in a planetary mixer. PDMS-based inks were printed the day after mixing.

Rheology. Dynamic frequency sweeps and dynamic strain sweeps were collected on an Ares-G2 rheometer. Sweeps were collected using 25 mm diameter parallel plates with a gap size of 1 mm. Oscillatory frequency sweeps were collected at a strain of 12.5%, from a frequency of 100 to 0.1 rad/s. Oscillatory amplitude sweeps were collected at a frequency of 10 rad/s from a strain of 1000 to 0.01%.

Interfacial Tension. Interfacial tensions were measured between oil-based inks and water-based supports using a Du Noüy ring force tensiometer (Sigma Instruments 700/701). Interfacial tensions between water-based inks and water-based supports were assumed to be negligible. For comparison, one test included Laponite and silica, but we could not confirm that elasticity had a negligible effect

https://doi.org/10.1021/acsami.2c08047
ACS Appl. Mater. Interfaces XXXX, XXX, XXX−XXX

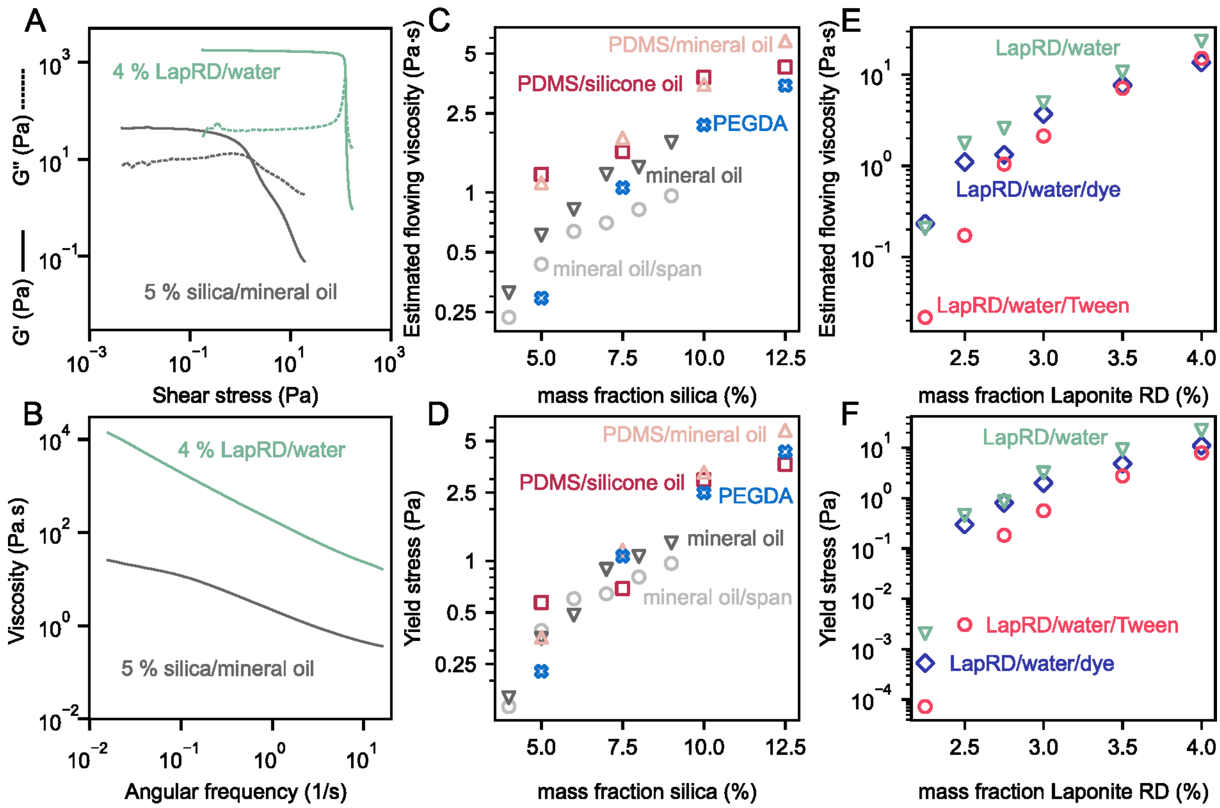

Figure 2. (A) Examples of oscillatory strain sweeps showing yield stress behavior for Laponite-based and silica-based fluids. (B) Examples of oscillatory frequency sweeps showing shear thinning behavior for Laponite-based and silica-based fluids. (C) Estimated ink viscosity inside nozzle as a function of silica mass fraction in ink, at ink speeds of 5 mm/s. (D) Measured yield stress as a function of silica mass fraction in ink. (E) Estimated support or ink viscosity inside nozzle as a function of Laponite mass fraction in support or ink, at ink speeds of 5 mm/s. (F) Measured yield stress as a function of Laponite mass fraction.

on the measurements, so interfacial tensions included in the scaling variables used data from fluids without Laponite and silica.

Printer Configuration. Experiments were conducted on a modified Shopbot Desktop D2418 CNC mill (Figure 1). The drill head was replaced by a stainless steel stage, which was cantilevered out from the gantry. The moving stage contained a gasket-lined slot that held a replaceable glass printing reservoir. The reservoirs were made of 75 mm by 25 mm by 1 mm glass slides, glued together using Loctite 0151 adhesive. All other components were static and fixed to the base of the printer. The nozzle was a 20 gauge blunt tipped needle with an inner diameter (d_i) of 0.603 mm, a wall thickness of 0.152 mm, and a length of 38 mm. A Fluigent LineUp Flow EZ mass flow controller controlled the ink flow rate via programmed air pressures. A color camera (Basler ace acA800-510uc) with a lens (VZM 450i) viewed the printing reservoir from the side. The reservoir was backlit by two LEDs at wavelengths of 590 and 625 nm, mounted together with a long-pass mirror and ground glass diffuser (Thorlabs). The gantry, mass flow controller, and camera were controlled using a custom interface written in Python.[48]

Densities, which were used in pressure−flow speed calibration, were collected by measuring masses of known volumes of ink. Each time a new ink was loaded onto the printer, extrusion pressures were calibrated to intended flow speeds by extruding ink into air at a fixed pressure for a fixed amount of time and measuring extruded masses. A quadratic curve was fit to the pressure−flow speed measurements and used to calculate extrusion pressures. For fumed silica-based inks, the quadratic term was usually negligible. Calibration curves for a given composition could vary between trials based on small variations in the time since mixing, length of the tubing, or composition.

Toolpaths were designed to print horizontal and vertical lines (Figure 1). First, five horizontal lines (10−15 mm) were printed such that the camera would view them head-on, documenting their cross-sectional shape (XS). The first printed line was not included in the reported data, to eliminate transient effects. Next, four vertical lines were printed (10−15 mm), wherein the nozzle would start at the top of the line, plunge to the bottom without extruding ink, then extrude ink as the nozzle traveled upward (vertical). Finally, three horizontal lines (17−22.5 mm) were printed such that the camera would record their side view. The extrusion pressure was turned off at the end of each line. For some experiments, the extrusion pressure was turned off slightly before the end of the line due to a machine error. Pressure curves were recorded during printing, so anticipated filament dimensions were calculated considering transients and timing inaccuracies.

Image Analysis. During each print, videos were collected of the printing process. After the print, the nozzle was removed, and images were collected. First, the entire horizontal area was imaged, from bottom to top and left to right. Next, vertical lines were imaged in reverse order from when they were printed, from bottom to top. Finally, cross-sections were imaged in reverse order, from bottom to top. For all filaments, the focal plane was in the center of the filament.

Images were processed using OpenCV 4.5.4[52] in Python 3.8.[53] The code for this work is available at ref 46. First, images were stitched together such that all of the horizontal lines combined into one image and each vertical and XS line had their own image. Stitching smaller images allowed for higher-resolution measurements, although, in some cases, the ink and support moved between images, particularly fluid combinations with dynamic processes including capillarity and swelling. Next, images were thresholded, filled, and labeled into connected components to identify unique ink segments. For cross-sections, the largest ink segment was selected and measured. For horizontal and vertical lines, where some lines ruptured into multiple droplets, the segments were separated by the line they belong to, counted, and measured.

Statistical analysis was performed using both linear regressions and Spearman rank correlations in Python. Unless otherwise noted, both variables are log-scaled before performing linear regressions. Spearman rank correlation coefficients, r_s, and p values are listed in the Supporting Information. To be considered as a potential scaling variable, $|r_s| > 0.5$. In all such cases, the p values are much less than 0.01. Throughout this work, error bars indicate standard error.

Simulations. For comparison and understanding of the pressure field, simulations from ref 29 and new simulations are shown in the Supporting Information. New simulations of Newtonian inks in Newtonian supports were run as described in ref 29 at support viscosities of 10^1 and 10^2 Pa·s and at ink viscosities of $10^{-0.5}$, $10^{0.5}$, $10^{1.5}$ $10^{2.5}$, $10^{3.5}$, and $10^{4.5}$ Pa·s. Briefly, OpenFOAM, a volume-of-fluid-based computational fluid dynamics solver, was used to simulate the extrusion of individual horizontal filaments from a static nozzle oriented along the z axis into a bath, where the surfaces of the bath are flowing along the x axis.[29,54] The nozzle has the same dimensions as the 20 gauge nozzle used in these experiments, and both print speeds are set to 10 mm/s (twice as fast as the default speed in the experiments). Cross-sections were collected from the simulated 3D volume 5 mm downstream of the nozzle after 2.5 s of extrusion and reported in the Supporting Information of this work and in ref 29. For vertical filaments, boundary conditions were established slightly differently. The positive and negative x and positive and negative y faces, which were parallel to the direction of flow, had a constant velocity downstream at 10 mm/s. The ink inlet, which was parallel to the direction of support flow, had a constant velocity downstream at 10 mm/s. The nozzle walls had a no slip boundary condition. The positive and negative z faces, orthogonal to the flow direction, were quasi-free surfaces like the positive z and downstream x face of the horizontal simulation, so support and ink could flow in and out.

■ RESULTS AND DISCUSSION

Particle Additives Control Rheology. We use particle additives to control the rheology of the ink and support, which strongly influence printability. For good form holding, a yield stress is helpful in both the ink and support, such that the fluids are solid-like below the yield stress and liquid-like above the yield stress. To limit the pressures required to extrude inks, and to allow the nozzle to travel through the bath without deflecting, shear thinning behavior is also beneficial. If the ink and support are shear thinning, they have a low viscosity within and near the nozzle and a high viscosity during recovery. All of the inks and supports in this study have a yield stress and shear thinning behavior above yield (Figure 2 and Supporting Information Figure S1), although in some cases the yield stress is very low. There are multiple ways one can define the yield stress.[55] We define the yield stress, τ_y, as the drop-off stress at which the storage modulus (G') decreases by 2% relative to the average G' measured at lower stresses. Another common way to define the yield stress is the crossover stress, where G' is equal to the loss modulus (G'').[55] The crossover stress is higher than the drop-off stress and is too high to properly describe the behavior of most Herschel−Bulkley fluids.[55] Using the drop-off stress from oscillatory strain sweeps, we fit the oscillatory frequency sweep data to the Herschel−Bulkley model: $\eta = \tau_y/\dot{\gamma} + k\dot{\gamma}^{n-1}$, where η is the viscosity, $\dot{\gamma}$ is the shear strain rate, k is the consistency index, and n is the power law index. Fitted regression values are shown in Figure 2 and Table S3. In the following sections, we use these fitted values to estimate local viscosities for the ink and support. Because these materials are shear thinning, their viscosities are non-uniform.[29] However, previous simulations indicated that the viscosities of the ink and support within a yielded zone near the nozzle only vary within an order of magnitude and can be estimated using the ink and support speeds and dimensions of the nozzle.[29] In the following sections, we use the Herschel−Bulkley model to estimate the viscosities of the support flowing around the nozzle at shear rate $\dot{\gamma}_{\mathrm{sup}} = v_{\mathrm{sup}}/d_{\mathrm{o}}$ and the ink flowing through the nozzle at shear rate $\dot{\gamma}_{\mathrm{ink}} = v_{\mathrm{ink}}/d_{\mathrm{i}}$.

Increasing the concentration of rheological modifier, whether it is Laponite RD, hydrophobic fumed silica, or hydrophilic fumed silica, increases the viscosity and yield stress of the support (Figure 2C,D). Adding Tween 80 or Nile Blue A dye to Laponite in water decreases the viscosity and yield stress (Figure 2E,F). Whereas Laponite-containing fluids exhibit a sharp G' drop-off at yield and large G'/G'' contrast below yield, the silica-containing inks experience a more gradual G' drop-off (Figure 2A and Figure S1). The oil-based inks exhibit less severe shear-thinning behavior than the water-based fluids, particularly at low strain rates (Figure 2B and Figure S1E−H). The Laponite-modified fluids also have a stronger dependence on the time since mixing than the fumed silica-modified fluids. Immediately after mixing, Laponite-modified fluids are pourable and have a low viscosity, allowing for support baths without air bubbles. However, within the first day, the viscosity and yield stress increase sharply and then continue to rise gradually over time (Figure S2A). In contrast, the rheology of silica-modified fluids varies less over time, particularly for high silica loadings (Figure S2B).

Composition Controls Interfacial Tension. We use different fluid matrices and surfactants to probe varying interfacial tensions. Interfacial tensions between water-based supports and water-based inks were assumed to be negligible. Interfacial tensions between water-based supports and oil-based inks, without Laponite RD and fumed silica, were measured using a Du Noüy ring force tensiometer (Table 2).

Table 2. Material Systems Used in This Work[a]

support composition	ink composition	symbol	σ (mN/m)
water, Laponite	water, Laponite, blue dye	water	0
water, Laponite	PEGDA, water, blue dye, silica	PEG	0
water, Laponite, Tween 80	mineral oil, Span 20, red dye, silica	MO/Span	1.42 ± 0.07
water, Laponite	mineral oil, red dye, silica	MO	42.13 ± 0.14
water, Laponite	PDMS, mineral oil, red dye, silica	PDMS/MO	32.76 ± 0.02
water, Laponite	PDMS, silicone oil, red dye, silica	PDMS/SO	56.28 ± 0.02

[a]Nonzero interfacial tensions and standard error are collected via Du Noüy ring tensiometry without Laponite and silica but with dyes. Uncertainty is standard error.

Adding Tween 80 to water and Span 20 to dyed mineral oil reduces the interfacial tension from 42.13 ± 0.14 to 1.42 ± 0.07 mN/m. PDMS with mineral oil has a lower interfacial tension than PDMS with silicone oil, although PDMS and the mineral oil phase separate, so this measurement may be more reflective of a single phase than the mixture. Laponite and silica may change the interfacial tension. When the support is freshly mixed water with 2% Laponite RD, and the ink is mineral oil with Sudan III dye and 4% silica, the measured interfacial tension rises to 53.54 ± 0.24 mN/m, from 42.13 ± 0.14 mN/m without rheological modifiers. The Pickering effect, i.e., interfacial stabilization via migration of particles to the interface, has been proposed as a mechanism for lowering

https://doi.org/10.1021/acsami.2c08047
ACS Appl. Mater. Interfaces XXXX, XXX, XXX−XXX

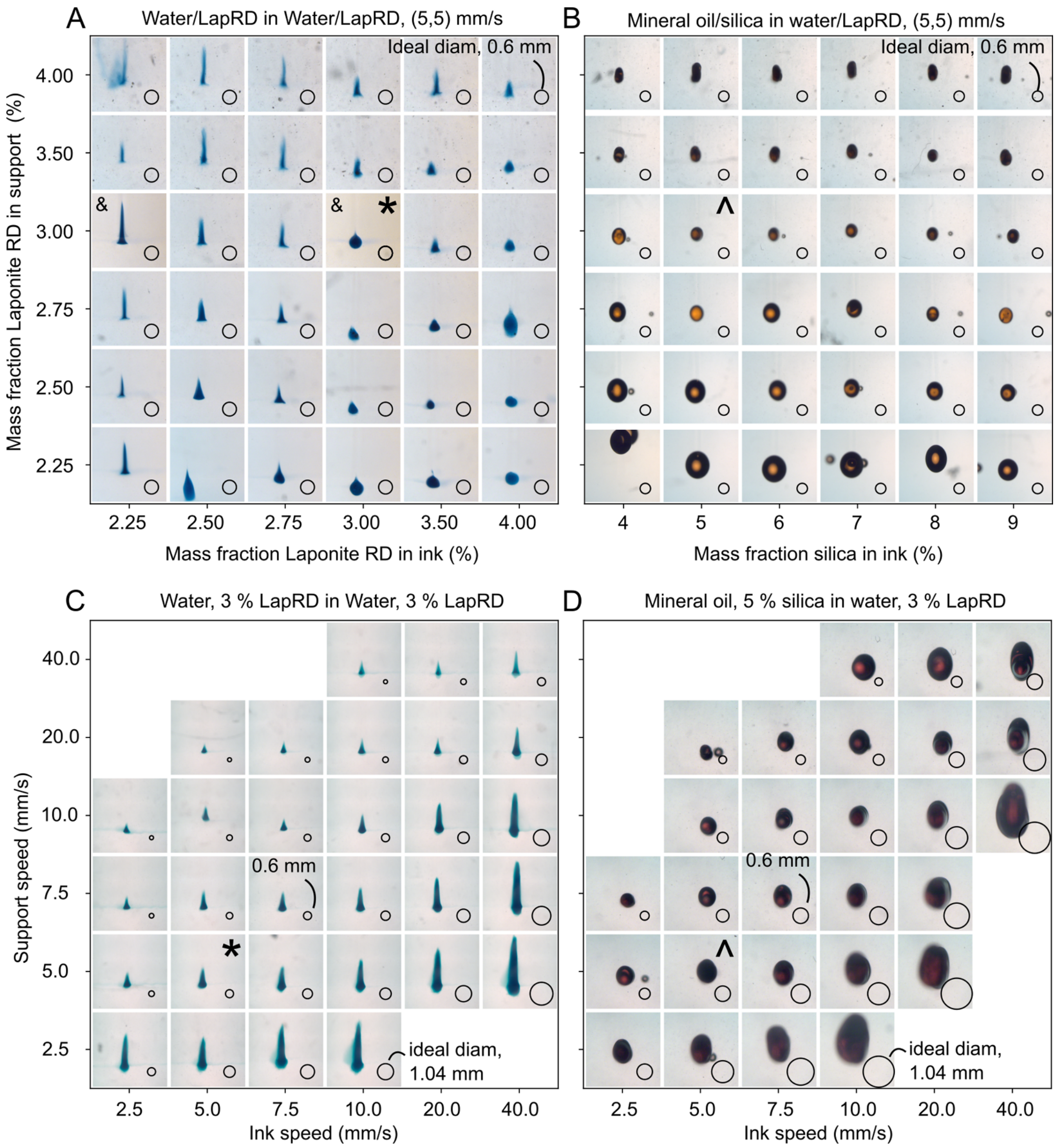

Figure 3. Cross-sections (XS in Figure 1). Circles indicate size of intended cross-section. (A, C) Laponite-based inks with blue dye in Laponite-based supports. Color variations are due to white balance. "*" indicates prints with the same parameters. (B, D) Mineral oil-based inks with red dye in Laponite-based supports. "∧" indicates prints with the same parameters. (A) Varying Laponite loadings in the ink and support, where the ink and support speeds are both 5 mm/s. "&" indicates prints which were done on a different day, with a new batch of materials. (B) Varying silica loadings in ink and Laponite loadings in support, where the ink and support speeds are both 5 mm/s. (C) Varying ink and support speeds, where ink and support have 3% Laponite. (D) Varying ink and support speeds, where the ink has 5% silica and the support has 3% Laponite.

interfacial tension in embedded 3D printing of viscoelastic materials,[32] and migration of particles to the ink−support interface has been leveraged to stabilize printing of Newtonian fluids with an otherwise high interfacial tension.[56,57] However, the Pickering effect would lower the measured interfacial tension,[58] while here the addition of particles raises the interfacial tension. It is possible that this increase in measured interfacial tension comes from elasticity or viscous dissipation, which are assumed to be negligible in Du Noüy ring tensiometry. As such, in the remainder of this work, we use interfacial tension measurements collected without fumed silica and Laponite.

Increasing Viscosity Ratio and Decreasing Capillary Number Produce Rounder Filaments. Head-on views of horizontal lines (XS in Figure 1) indicate that rheology, interfacial tension, and print speeds all have a considerable impact on the morphology of filaments. It is not safe to assume that cross-sections will be circular. A common morphology at zero interfacial tension is a fin-shaped morphology, wherein the top of the filament is pinched into a sharp edge and the bottom of the filament is wider and either rounded or flat (Figure 3A,C). At nonzero interfacial tension, cross-sections do not have sharp edges and tend to be circular or elliptical (Figure 3B,D).

The concentrations of rheological modifier in the ink and support, which correlate with the local viscosity and yield stress, influence filament shapes. When printing water−Laponite inks into water−Laponite baths, different Laponite loadings produce a wide range of filament shapes (Figure 3A). Where there is much more Laponite in the ink than in the support, nearly circular filaments are produced, with slight pinching at the top of the filament (Figure 3A). In contrast,

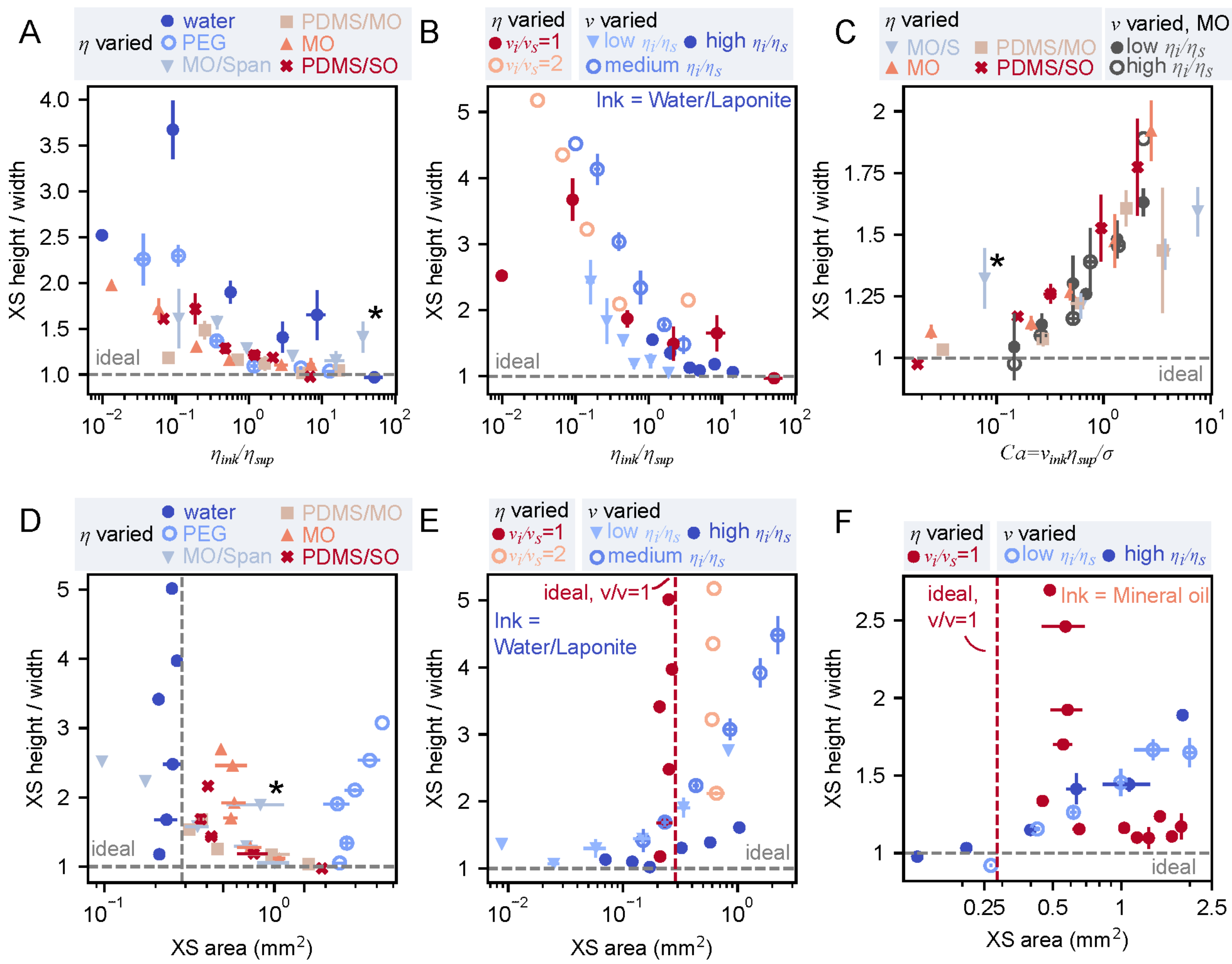

Figure 4. Cross-section aspect ratios. Error bars indicate standard error. * includes curling instabilities. (A) Viscosity ratio vs aspect ratio, where the velocity ratio is 1. (B) Viscosity ratio vs aspect ratio, for water-/Laponite-based inks, where either viscosities or speeds are varied. (C) Capillary number vs aspect ratio, where interfacial tension is nonzero and either viscosities or speeds are varied. (D−F) Cross-sectional area vs aspect ratio. (D) Viscosity sweeps, where the speed ratio is 1. (E) Viscosity and speed sweeps, for water/Laponite inks. (F) Viscosity and speed sweeps, for mineral oil-based inks.

where the Laponite loading is much higher in the support than in the ink, the filaments are tall and narrow with a sharp, pinched top edge and a flat bottom face (Figure 3A). When printing mineral oil−silica inks into water−Laponite baths, filaments tend to be rounder (Figure 3B). Like the water-based inks, at low support viscosities and high ink viscosities, filaments are round, and at high support viscosities and low ink viscosities, filaments are tall and narrow (Figure 3B). However, the mineral oil-based filament cross-sections are smooth and do not exhibit the flat bottom edges and sharp top edges exhibited at zero interfacial tension. As shown in Figure S9, water-based cross-sections are more bottom-heavy. At nonzero interfacial tensions, the filament cross-sections are larger than intended due to shrinkage and rupture.

The ink and support speeds can also influence horizontal cross-sectional shapes. Here, the support speed is defined as the translation speed of the stage, and the ink speed is defined as the volume flux of ink divided by the inner cross-sectional area of the nozzle, as measured during calibration. The ink speed to support speed ratio influences both the cross-sectional area of the filament and its shape. Consider 3% Laponite in water inks extruded into 3% Laponite in water supports, which produce a triangular cross-section at a speed ratio of 1. Increasing the ink speed or decreasing the support speed increases the cross-sectional area, produces a rounder filament bottom surface, and produces a taller, sharper filament top edge (Figure 3C). Next, consider 5% silica in mineral oil inks extruded into 3% Laponite in water supports, which produce round cross-sections at a speed ratio of 1. Increasing the ink speed or decreasing the support speed leads to a larger cross-section and taller aspect ratio, still with round edges (Figure 3D).

To quantify the effects of printing parameters on cross-sectional shape, we can use the aspect ratio, defined as the height divided by the width of the bounding box containing the cross-section. We can use Spearman rank correlations to identify unifying scaling relationships across different material systems. A Spearman rank correlation coefficient, r_s, of −1 or 1 indicates a strong correlation, while a value of 0 is a weak correlation. At zero interfacial tension, the Reynolds number ratio (r_s = **0.76**), Bingham number ratio (r_s = **−0.75**), and viscosity ratio (r_s = **−0.77**) have similarly strong correlations with the cross-sectional aspect ratio (Table S4). All three scaling parameters contain the viscosity ratio, indicating that within the tested domain, the cross-sectional shapes change over speed sweeps not because of inertia but because the viscosity ratio decreases as the speed ratio increases (Figure S3). Increasing the viscosity ratio produces more circular filaments (Figure 4A,B), in agreement with previous simulations (Figure S4). Considering only water-/Laponite-based inks, both speed sweeps and viscosity sweeps collapse onto a similar curve (Figure 4B), confirming that the local viscosity ratio alone is sufficient to predict aspect ratios. Considering all interfacial tensions, for each ink, the aspect ratio decreases with increasing viscosity ratio (Figure 4A). At lower interfacial tensions, aspect ratios are larger (Figure 4A). One ink, mineral oil with surfactant, experiences an increase in measured aspect ratio at high viscosity ratios. In contrast with the pinching experienced at low viscosity ratios, this high aspect ratio represents a separate mechanism, where the filament curls over on itself near the nozzle (Figure S7). These curling instabilities were documented in simulations of Newtonian inks and supports at high viscosity ratios,[29] and they were more extensively explored via simulations and experiments in ref 59.

At nonzero interfacial tension, the interfacial capillary number, Ca (r_s = **0.67**), normalized support critical diameter, $\overline{d_{PR,sup}}$ (r_s = **0.68**), support Ohnesorge number, Oh_{sup} (r_s = **0.63**), Reynolds number ratio, Re_{ink}/Re_{sup} (r_s = **0.56**), and viscosity ratio, η_{ink}/η_{sup} (r_s = **−0.51**) correlate with the cross-section aspect ratio. The correlations with the Re ratio and viscosity ratio are weaker, indicating that the interfacial tension is necessary to predict the aspect ratio. The strongest correlations are with Ca and $\overline{d_{PR,sup}}$, indicating that the relationship between the print speed, rheology, and interfacial tension is a useful predictor of the aspect ratio. Increasing Ca increases the aspect ratio, indicating that filaments become more cylindrical with increasing interfacial tension, decreasing ink speed, and decreasing support viscosity (Figure 4C). The aspect ratio scales the same with Ca for speed sweeps and viscosity sweeps (Figure 4C and Figure S6A), while the aspect ratio increases more quickly with $\overline{d_{PR,sup}}$ for speed sweeps than viscosity sweeps (Figure S6D), indicating that Ca better captures the scaling of the system.

Cross-Sectional Shape Changes with Cross-Sectional Area. When the cross-sectional area increases, the cross-sectional shape changes. This is most apparent when plotting the cross-section aspect ratio directly against the cross-sectional area. First, consider only speed ratios of 1, with varying viscosities (Figure 4D). In water-/Laponite-based inks, the cross-sectional areas are all close to the intended area but have varying aspect ratios, indicating that changes in shape can occur without a change in area. Next, consider PEGDA-based inks. All of these inks have roughly 14 times larger areas than intended. In PEGDA-based inks, there is a positive correlation between the cross-sectional area and the aspect ratio. Finally, consider oil-based inks. There is a negative correlation between cross-sectional area and aspect ratio. Where the cross-sectional area is close to the intended area, aspect ratios are taller than intended, and where the areas are largest, filaments are circular.

Next, consider how viscosity sweeps vary from speed sweeps when comparing cross-sectional areas and aspect ratios. Consider water-/Laponite-based inks at zero interfacial tension (Figure 4E). Whereas viscosity sweeps can produce a variety of aspect ratios at the same area, speed sweeps exhibit a positive correlation between cross-sectional area and aspect ratio. As the area increases due to the increase in speed ratio, that extra area is diverted vertically. Next, consider mineral oil-based inks (Figure 4F). For speed sweeps, as the extruded area increases, that extra area is diverted vertically, like the zero interfacial tension case. However, for viscosity sweeps, there is a negative correlation between area and aspect ratio. For viscosity sweeps, the cross-sectional area also increases as horizontal lines get shorter (Figure S8), indicating that the increase in area and decrease in aspect ratio both come from contraction of the filament toward a spherical shape. In contrast, for speed sweeps, cross-sectional areas increase while horizontal lines get longer. Thus, increased speed ratios lead to larger areas but less contraction (Figure S8).

Swelling Effects on Shape and Size of Cross-Section. PEGDA-based inks show that swelling can increase the size and decrease the aspect ratio of filament cross-sections. These PEGDA-based inks are 52.5−57% water, in contrast with the Laponite/water supports, which are 96−97.75% water. The measurements in Figure 4 are collected roughly 4 min after printing. As shown in Figure 4D and Figure 5, those cross-sections are much larger than intended. However, comparing images collected just after the line is printed to images collected after 4 min, the cross-section clearly evolves over time. Just after printing, cross-sections are only slightly larger than the intended cross-section (Figure 5). Like the water/Laponite inks in Figure 3A, the PEGDA cross-sections just

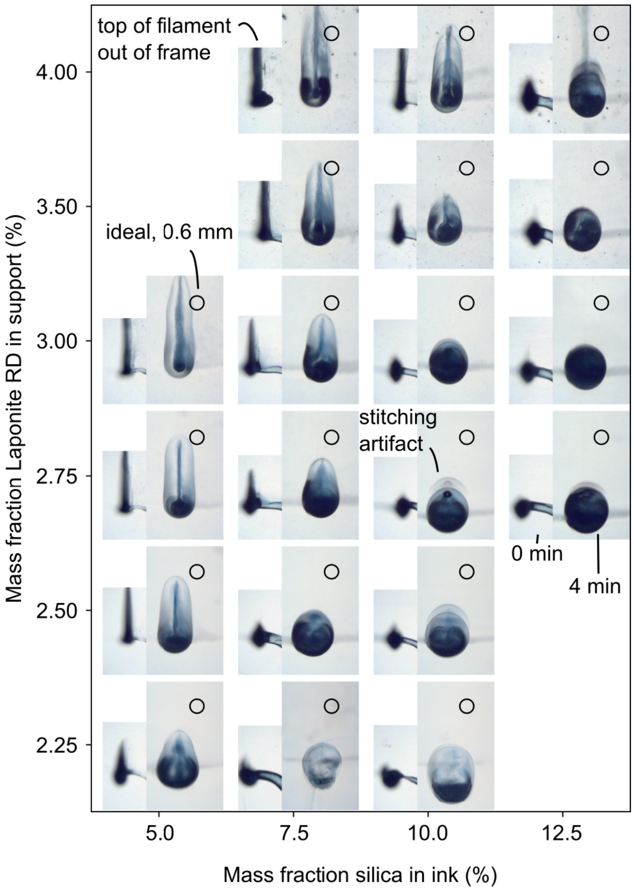

Figure 5. Cross-sections of PEGDA-based inks in water−Laponite supports. Images on left were collected immediately after printing, with the focal plane at the end point of the line closest to the camera. Images on right were collected approximately 4 min after printing, with the focal plane in the center of the line. In some images, an ink thread exists between the filament and the nozzle.

https://doi.org/10.1021/acsami.2c08047
ACS Appl. Mater. Interfaces XXXX, XXX, XXX−XXX

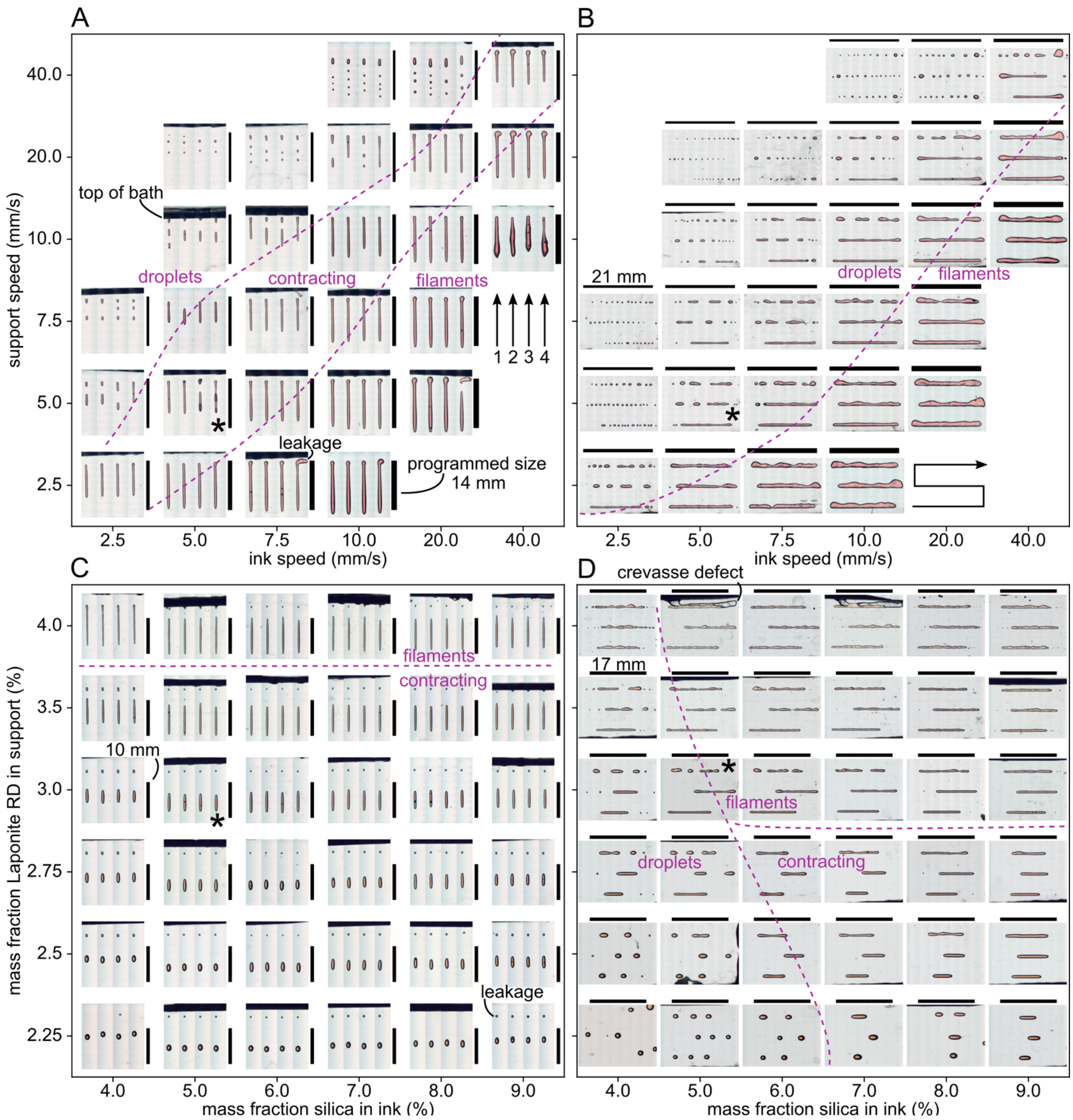

Figure 6. Images of vertical and horizontal lines (as named in Figure 1), where the ink is mineral oil-based. Lines can be either continuous filaments with accurate length (filaments), contracting into short filaments (contracting), or rupturing into multiple droplets (droplets). Approximate domain boundaries are shown. * indicates images which used the same speeds and materials. (A, C) Images of vertical lines, cropped together. Interline spacing is wider in the actual bath. (B, D) Horizontal lines. (A, B) Speed sweeps at 5% silica in the ink and 3% Laponite in the support. Pressures were on for the entire line length. (C, D) Viscosity sweeps at ink and support speeds of 5 mm/s. Pressures were turned off just before the end of the line.

after printing are more circular at higher viscosity ratios. However, swelling slightly decreases the aspect ratios over time, as large aspect ratios expose the sides of the filament so they are available for swelling, so widths increase more quickly than heights. Swelling of the filament sides is likely why cross-sectional aspect ratios are smaller for PEGDA inks than for water/Laponite inks (Figure 4A), even though both are water-soluble and have negligible interfacial tensions. Likewise, swelling at the sides of the filament is likely why cross-sectional areas increase with aspect ratio in PEGDA (Figure 4D).

Increasing Capillary Number Inhibits Rupture and Contraction. At nonzero surface tension, the length of printed filaments and droplets scales with the capillary number. Lengths are important for shape fidelity. If filaments contract to a shorter length than programmed and contraction is not taken into account during toolpath design, then filaments will be written in the wrong relative positions. Even if contraction is taken into account, contraction over nontrivial time scales will complicate the toolpath design. Moreover, contraction decreases the resolution of the print because it produces thicker filaments. In embedded droplet printing, where droplets are intentionally produced, the droplet size is critical for many applications.

Viewing filaments from the side, it is evident that printing direction, print speeds, and ink and support rheology influence the morphology of the filament. Printed lines exhibit three types of morphologies: droplets, contracting, and filaments (Figure 6). Droplets occur where multiple droplets rupture from the nozzle over the course of the printed line or where a printed filament ruptures into droplets after printing. Contracting filaments only rupture from the nozzle at the end of printing but are shorter than the intended filament length. Filaments are the intended length.

Morphology maps vary depending on whether speeds or viscosities are varied and whether lines are vertical or horizontal. First, consider speed sweeps. Filaments occur at

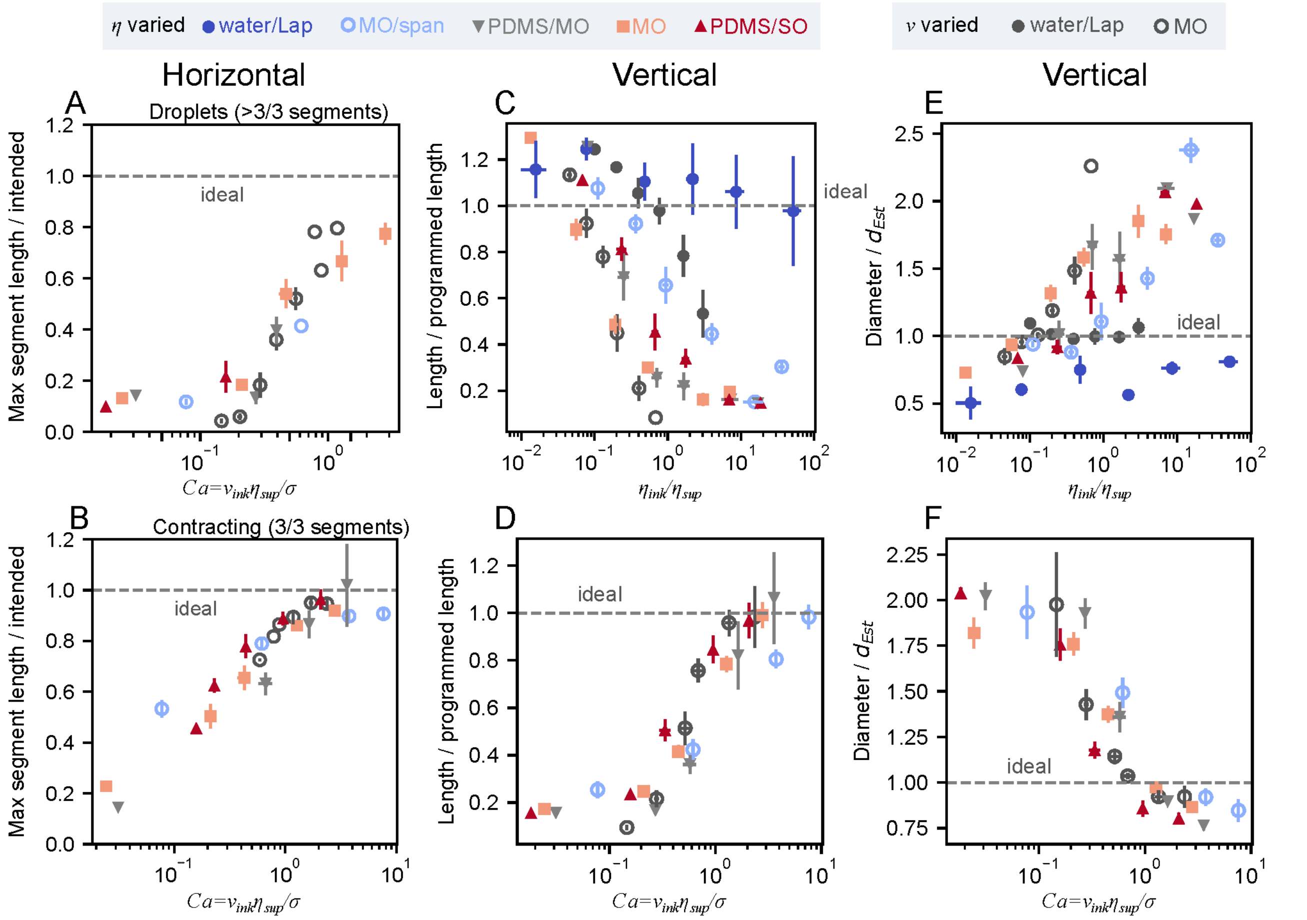

Figure 7. (A, B) Lengths of longest horizontal segment, divided by programmed line length, for nonzero interfacial tensions. (A) Droplets, where there are more than 3/3 segments. (B) Contracting filaments, where there are 3/3 segments. (C−F) Normalized vertical line lengths and widths, for viscosity and speed sweeps. (C) Viscosity ratio vs normalized length. (D) Capillary number vs normalized length. (E) Viscosity ratio vs normalized diameter. (F) Capillary number vs normalized diameter. Error bars indicate standard error.

high speed ratios, and droplets occur at low speed ratios (Figure 6A,B). However, vertical filaments are less prone to rupture. At intermediate speed ratios, vertical filaments contract, while horizontal filaments rupture into multiple droplets. Next, consider viscosity sweeps (Figure 6C,D). In vertical lines, filaments are produced at high support viscosities and contracting filaments are produced at low support viscosities. In horizontal lines, the same is true, but full length filaments start to appear at lower support viscosities, and there is a third region at low ink viscosities where droplets form. These phase boundaries indicate that horizontal lines suppress contraction, while vertical lines suppress rupture. Speed and viscosity sweeps also exhibit different dropletting behaviors. Because the ink flow speed becomes much slower than the support translation speed, filaments break up into more, smaller droplets, as droplets rupture from the nozzle more frequently (Figure 6A,B). In contrast, as the ink becomes much less viscous than the support, filaments break up into fewer, larger droplets, as droplets cling to the nozzle and are dragged through the matrix (Figure 6D).

There are two ways we can quantify the horizontal line length. The sum of the segment lengths in each line represents the accumulated shrinkage of all of the extruded material. The maximum segment length in each line represents the size of individual droplets. For both metrics, the length is normalized by the distance traveled while the extrusion pressure was on, i.e., the expected length of the filament. Horizontal line lengths and droplet lengths at zero interfacial tension are close to the intended line length (Figure S12) and do not correlate with any of the tested variables (Table S7, Table S6). However, line lengths vary at nonzero interfacial tension.

First, consider the dropletting region, where more than 1 segment per line is extruded (Figure 7A). Droplet lengths decrease with decreasing Ca and, then, plateau around $Ca <$ 0.1 to 3−10% of the intended length. Several variables have strong r_s with the maximum segment length: Ca (r_s = **0.87**), $\overline{d_{PR,ink}} \times \overline{d_{PR,sup}}$ (r_s = **0.83**), Oh_{sup} (r_s = **0.72**), Re_{ink}/Re_{sup} (r_s = **0.64**), and η_{ink}/η_{sup} (r_s = **−0.55**) (Table S8). Of those, Ca and followed by the product of the ink and support normalized critical diameters have the strongest correlation with line length. While the droplet length increases with Ca at a similar rate for speed sweeps and viscosity sweeps, the droplet length scales much faster with $\overline{d_{PR,ink}} \times \overline{d_{PR,sup}}$ for speed sweeps than viscosity sweeps (Figure S13), indicating that Ca better represents the scaling of the system.

Next, consider horizontal line lengths in the contracting and filament regions, where one continuous segment is produced for each intended line. Naturally, these contracting filaments are longer than the droplet maximum lengths, given the same Ca (Figure 7A,B). However, for the same Ca, the sum of the droplet lengths is similar to the contracting filament length

https://doi.org/10.1021/acsami.2c08047
ACS Appl. Mater. Interfaces XXXX, XXX, XXX−XXX

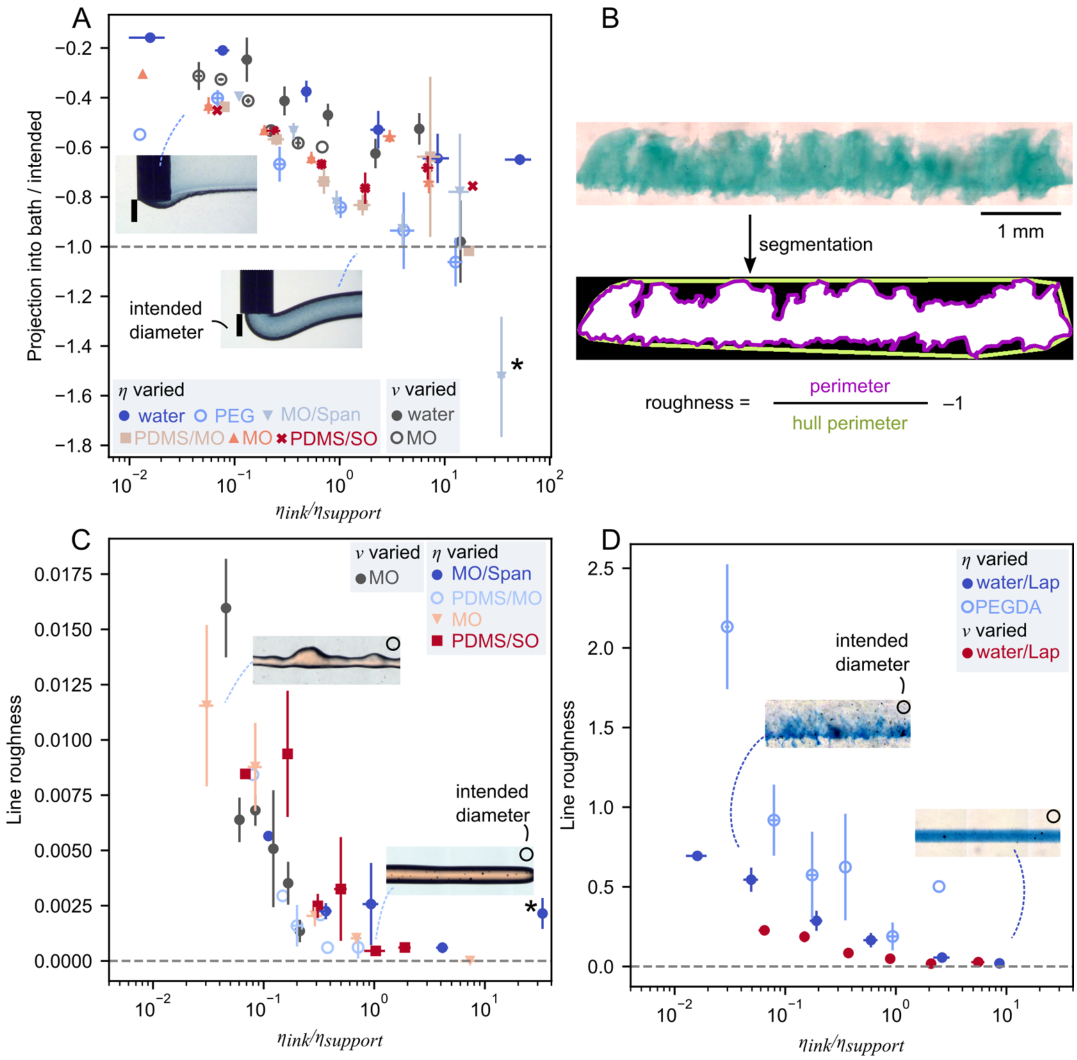

Figure 8. Filament position and roughness. * includes curling instabilities. (A) Depth of projection into the bath just below the nozzle, divided by d_{est}, the intended filament diameter. Negative projections are deeper into the bath. Insets are for PEGDA. (B−D) Roughness, represented by the object perimeter divided by the convex hull perimeter, where there are 3/3 segments. (B) Example of roughness calculation for a single water/Laponite segment. (C) Nonzero interfacial tensions. Insets are for mineral oil viscosity sweeps (MO). (D) Zero interfacial tension. Insets are for water/Laponite viscosity sweeps.

(Figure S14). Like droplet lengths, contracting filaments lengths increase with increasing Ca (Figure 7B). Several variables have strong r_s with the total line length: Ca (r_s = **0.90**), $\overline{d_{PR,sup}} \times \overline{d_{PR,ink}}$ (r_s = **0.84**), Oh_{sup} (r_s = **0.77**), Re_{ink}/Re_{sup} (r_s = **0.72**), and η_{ink}/η_{sup} (r_s = **066**) (Table S9). Like the maximum segment length, the total line length correlates most strongly with Ca, followed by the product of the normalized critical diameters. Between the two, Ca better consolidates viscosity sweeps and speed sweeps onto the same trendline (Figure S15A,B).

There is no critical capillary number or normalized critical diameter at which droplets begin to appear. While droplets tend to appear at lower Ca and $\overline{d_{PR,sup}}$ values, in all of the tested materials, there are Ca and $\overline{d_{PR,sup}}$ values where both contracting filaments and droplets are present (Figure S14). By mapping morphologies as a function of support yield stress and 1/(estimated radius), it is apparent that the proposed critical radius of σ/τ_y does not hold over short time scales, as the filament and droplet regions of the map overlap greatly (Figures S16 and S17). Like the results in ref 32, a much lower apparent interfacial tension than the measured interfacial tension would be necessary to bring the continuous filaments on the correct side of the critical radius curve (Figures S16 and S17).

Vertical line lengths follow patterns similar to horizontal line lengths. Vertical filament lengths are slightly shorter than contracting horizontal lengths given the same Ca, for each material system (Figure S14). This difference is more pronounced for viscosity sweeps than for speed sweeps. Like horizontal lines, vertical line lengths increase with capillary number (Figure 7D). However, unlike horizontal lines, vertical lines at zero interfacial tension are not always the correct length. Instead, the zero interfacial tension vertical lines are typically longer than intended (Figure 7C). Though it appears that at zero interfacial tension, line lengths decrease with increasing viscosity ratio, the correlation between viscosity ratio and line length is weak (r_s = −0.18; p = 0.07) (Figure 7C and Table S10). For some vertical lines, including the water/Laponite viscosity sweep in Figure 7C, after the extrusion pressure dropped to zero, the stage continued to translate

https://doi.org/10.1021/acsami.2c08047
ACS Appl. Mater. Interfaces XXXX, XXX, XXX−XXX

downward, allowing extra fluid to leak out of the nozzle even at zero extrusion pressure. In nonzero interfacial tension fluids, the maximum recorded line length is close to the intended line length and the fluid breaks off of the nozzle when flow stops. Leakage after the pressure drop manifests as a small droplet that clings to the nozzle and breaks off when the nozzle starts to travel horizontally again (Figure 6C).

Vertical line lengths correlate with many of the same scaling parameters as horizontal line lengths. At zero interfacial tension, there are no strong correlations between vertical line lengths and Re, Bm, or η (Table S10). For the speed sweep, the normalized length decreases with viscosity ratio, partly because the lines become too thin to detect (Figure S18). At nonzero interfacial tension, several variables have strong r_s with the vertical line length: Ca (r_s = **0.87**), $\overline{d_{PR,sup}}$ (r_s = **0.85**), Oh_{sup} (r_s = **0.83**), Re_{ink}/Re_{sup} (r_s = **0.68**), $Bm_{ink}Bm_{sup}$ (r_s = **0.51**), and η_{ink}/η_{sup} (r_s = **−0.65**) (Table S11). Again, Ca has the strongest correlation, followed by $\overline{d_{PR,sup}}$.

At zero interfacial tension, vertical line diameters are constant. The water-based ink viscosity sweep diameters are smaller than intended, which may be connected to transients, the calibration process, or inaccurate image segmentation at the diffuse interface. Intuitively, at nonzero interfacial tension, vertical line diameters grow wider as vertical line lengths shrink, with increasing viscosity ratio (Figure 7E) and decreasing Ca (Figure 7F). At nonzero interfacial tension, familiar correlations with the vertical line diameter emerge: Ca (r_s = **−0.84**), $\overline{d_{PR,sup}}$ (r_s = **−0.88**), Oh_{sup} (r_s = **−0.85**), Re_{ink}/Re_{sup} (r_s = **−0.64**), $Bm_{ink}Bm_{sup}$ (r_s = **−0.61**), and η_{ink}/η_{sup} (r_s = **0.62**) (Table S13). Again, the strongest correlations are measured for Ca, $\overline{d_{PR,sup}}$, and Oh_{sup}. Because the correlation with Oh is no stronger than the correlation with Ca, inertia likely has a negligible impact on the vertical filament diameter at nonzero interfacial tension. Because the correlation with $\overline{d_{PR,sup}}$ is stronger than the correlation with Ca, it is possible that yielding has a greater impact on vertical filament diameter than viscous dissipation.

Increasing Viscosity Ratio Plunges Filament Deeper into Bath. The viscosity ratio controls vertical filament positioning, which is important for print feasibility. If the filament is positioned too high, the nozzle may need to scrape into existing lines to write new lines. Just below the nozzle, the ink projects into the bath, and just behind the nozzle, the filament rises (Figure 8A). The normalized projection into the bath is measured here as the z distance between the bottom of the nozzle and the part of the filament that projects deepest into the bath, divided by the estimated filament diameter d_{est}. A negative projection is into the bath, below the nozzle. Ideally, normalized projections should have a value of −1, indicating that the bottom of the filament is exactly one intended diameter below the nozzle. Most measured projections are greater than −1, indicating that the filament is scraped downstream, rather than projecting into the bath (Figure 8A). Projections become deeper with increasing viscosity ratio. In other words, viscous inks project deeply into low-viscosity baths.

There are several scaling variables that correlate strongly with the projection depth, but the viscosity ratio is the dominant scaling variable. For water-based inks, the projection depth strongly correlates with Re_{ink}/Re_{sup} (r_s = **0.68**) and η_{ink}/η_{sup} (r_s = **−0.69**) (Table S14). Because the strength of the correlation with Re_{ink}/Re_{sup} is no better than the strength of the correlation with the viscosity ratio, inertia is not necessary to explain differences in projection depth between inks, only viscous dissipation. At nonzero interfacial tension, there are many strong correlations with the projection depth: Ca_{ink}/Ca_{sup} (r_s = **−0.70**), $\overline{d_{PR,ink}}/\overline{d_{PR,sup}}$ (r_s = **−0.68**), Oh_{ink}/Oh_{sup} (r_s = **−0.78**), Re_{ink}/Re_{sup} (r_s = **0.77**), Bm_{ink}/Bm_{sup} (r_s = **−0.60**), and η_{ink}/η_{sup} (r_s = **−0.78**) (Table S15). The commonality among these ratios is that they all contain the viscosity ratio and/or yield stress ratio, and none contain the interfacial tension.

The vertical position of the filament downstream of the nozzle was also analyzed (Supporting Information). There are no clear, unifying trends across all inks. An experiment that explicitly controls for ink density and nozzle wetting may be necessary to better understand the scaling of the final vertical position of the filament.

Increasing Viscosity Ratio Decreases Roughness. Roughness is a critical metric of print quality. Surface roughness on an individual filament could lead to porosity, encapsulated support material, or surface roughness on the final part. To measure roughness, we use segmentation to binarize images of horizontal lines (Figure 8B). Roughness is measured as the perimeter of the filament divided by the perimeter of the convex hull that encompasses the filament, subtracted by 1. A roughness of 0 is perfectly smooth, with a convex hull that overlaps with the filament. A large roughness indicates that the filament contains deep and frequent crevices. Roughness primarily appears on horizontal filaments. At speeds and fluid compositions where horizontal filaments exhibit deep crevices, vertical filaments are smooth (Figure S26).

Filaments at nonzero interfacial tension are 2 orders of magnitude smoother than filaments at zero interfacial tension (Figure 8C,D). While filaments at nonzero interfacial tension can produce bulging filaments (Figure 8C), filaments at zero interfacial tension can produce fine protrusions with bulging end points, resulting in a very large surface area (Figure 8D). At both zero interfacial tension and nonzero interfacial tension, the filament roughness trends close to zero as the ink becomes more viscous than the support (Figure 8C,D). At very high viscosity ratios, the filament curls over on itself, as demonstrated in Figure S7 and ref 29. Because of the way roughness is defined, high viscosity ratio curling instabilities are measured as an increase in roughness but are governed by a different mechanism than the low viscosity ratio roughness measurements.

The filament roughness mainly scales with the viscosity ratio and capillary number. At zero interfacial tension, the horizontal line roughness correlates with Re_{ink}/Re_{sup} (r_s = **0.69**), Bm_{ink}/Bm_{sup} (r_s = **−0.73**), and η_{ink}/η_{sup} (r_s = **−0.78**). Of the three, the strongest correlation is with the viscosity ratio, indicating that yielding and inertia are not necessary to predict filament roughness at zero interfacial tension. At nonzero interfacial tension, the filament roughness correlates with Ca (r_s = **0.68**), $\overline{d_{PR,sup}}$ (r_s = **0.69**), Oh_{ink}/Oh_{sup} (r_s = **−0.70**), Re_{ink}/Re_{sup} (r_s = **0.73**), Bm_{ink}/Bm_{sup} (r_s = **−0.54**), and η_{ink}/η_{sup} (r_s = **−0.70**). Though Ca and $\overline{d_{PR,sup}}$ have similar correlation strengths, again, Ca better collapses speed sweeps and viscosity sweeps onto the same curve than $\overline{d_{PR,sup}}$ (Figure S27D,E). Although water-based inks experience much higher roughnesses, between oil-based inks, we found no scaling relationship

https://doi.org/10.1021/acsami.2c08047
ACS Appl. Mater. Interfaces XXXX, XXX, XXX−XXX

which better unifies inks of different interfacial tension than the viscosity ratio (Figure S27D−I). Moreover, because Oh_{ink}/Oh_{sup}, Re_{ink}/Re_{sup}, and η_{ink}/η_{sup} all contain the viscosity ratio, it is likely that viscous dissipation alone is sufficient to explain differences in roughness.

Multiple Hypotheses Probe Physics of Defect Formation. A summary of the key scaling relationships is shown in Table 3. Out of the tested variables, the viscosity ratio is the dominant scaling variable at zero interfacial tension for the cross-section aspect ratio, projection depth, and horizontal line roughness. At nonzero interfacial tension, the capillary number and normalized critical diameter have similar correlation strengths, with the capillary number often exhibiting slightly stronger correlations and better unification of speed sweeps and viscosity sweeps, for the cross-section aspect ratio, horizontal segment length, total horizontal line length, vertical line length, and vertical line diameter. Even at nonzero interfacial tension, the viscosity ratio is sufficient to describe the scaling of projection depth and horizontal line roughness.

Table 3. Summary of Key Spearman Rank Correlation Coefficients between Printing Metrics and Scaling Variables

	$\sigma = 0$		$\sigma > 0$		
metric	η_{ink}/η_{sup}	Re_{ink}/Re_{sup}	Ca	$\overline{d_{PR,sup}}$	η_{ink}/η_{sup}
XS aspect ratio	**−0.77**	0.76	**0.67**	**0.68**	**−0.51**
horizontal segment length	0.00	0.02	**0.87**	**0.76**	**−0.55**
total horizontal length	−0.02	0.44	**0.90**	**0.82**	**−0.66**
total vertical length	−0.40	0.45	**0.87**	**0.85**	**−0.65**
vertical line diameter	0.16	−0.12	**−0.84**	**−0.88**	**0.62**
projection depth	**−0.69**	**0.68**	0.34	0.52	**−0.78**
horizontal roughness	**−0.78**	**0.69**	**0.68**	**0.69**	**−0.70**

The Spearman rank correlation tables in the Supporting Information illustrate the importance of testing multiple hypotheses. For example, we could hypothesize that because Oh is a strong predictor of dropletting in inkjet printing, Oh could also be a strong predictor of dropletting in embedded 3D printing. If we only probed Oh, we would see that p values of Spearman rank correlations between Oh and line lengths are very small, down to orders of 10^{-30}. From that single correlation, we could erroneously conclude that the balance between viscous dissipation, inertia, and interfacial tension is critical. However, by testing both Ca and Oh, we can see that Ca has an even stronger correlation. Thus, the strength of the Oh correlations likely comes from its similarity to Ca, so inertia is not important at these low Reynolds numbers, just the relationship between viscous dissipation and interfacial tension.

Viscosity Ratio Controls Defects at Zero Surface Tension. At zero interfacial tension, the dominant scaling variable is the viscosity ratio. Helpfully, when printing horizontal lines, increasing the η_{ink}/η_{sup} produces rounder, smoother filaments that project more deeply into the bath. Correlations between the measured defect sizes and the Bingham numbers and Reynolds numbers are the same strength or weaker than correlations with the viscosity ratio, indicating that yielding and inertia have a negligible effect compared to viscous dissipation within the probed regime. The correlations between viscosity ratio and roundness and viscosity ratio and projection depth are consistent with simulations of embedded 3D printed filaments.[29] Where decreasing the ink pressure increases the ink viscosity and increasing translation speeds decrease the support viscosity, these results are consistent with previous experimental findings, which indicated that increasing the ink pressure increased aspect ratios,[10] increasing the translation speed decreased aspect ratios,[10,30] and increasing the ink pressure to translation speed ratio increased aspect ratios.[6] Similarly, other works found that more viscous baths produce larger filament cross-section aspect ratios[18,27,28,60] and teardrop or fin-shaped cross-sections,[27] and more viscous inks produce smaller aspect ratios.[60] Additionally, sharp edges and triangular cross-sections such as those shown in Figure 3A,C have been demonstrated for water-based inks in water-based supports.[23,27,30] Our findings provide a general rule for material and speed selection: to produce smooth, circular filaments, the local viscosity of the ink in the nozzle should be slightly higher than the local viscosity of the support flowing around the nozzle. However, if the viscosity ratio is too high, curling instabilities emerge.

Saffman-Taylor Instabilities Cause Roughness. At low ink viscosities and high support viscosities, surface roughness appears on filaments, particularly at low interfacial tension. Previous reports of varying roughness in different microgels could be linked to the varying viscosities of the supports or varying support particle size.[14,31,33] Because a low viscosity fluid is injected into a viscous fluid, this material system is consistent with Saffman−Taylor instabilities.[61] An increase in interface length with decreasing viscosity ratio matches simulations of Saffman−Taylor instabilities.[62] At nonzero interfacial tension, the increase in roughness with capillary number is consistent with previous findings that Saffman−Taylor instability finger width decreases with increasing capillary number.[63] Although oil-based inks demonstrate much lower roughness values than water-based inks, between oil-based inks the interfacial tension does not seem to have a strong effect on roughness, so roughness may correlate more strongly with miscibility or roughness may plateau with respect to interfacial tension above a critical interfacial tension.

The trends in surface roughness are more consistent with Saffman−Taylor instabilities than other instabilities that appear in extrusion-based printing processes. One is the Plateau−Rayleigh instability, wherein interfacial tension causes perturbations on the surface of a filament to propagate, causing the filament to rupture into droplets.[2] A Plateau−Rayleigh instability can increase the surface roughness of a filament by initiating but not completing pinch-off. Slight increases in surface roughness associated with incomplete Plateau−Rayleigh instabilities are apparent in these experiments at low capillary numbers which are not low enough to induce pinch-off (Figure S28). However, Plateau−Rayleigh instabilities become more prominent at low capillary numbers, while the surface roughness increases with capillary number (Figure S28). Another potential source of roughness is an extrusion instability such as a sharkskin instability. These instabilities appear at the nozzle exit for polymer melts extruded into air and become more severe with increasing flow rate.[64] Sharkskin instabilities originate directly at the nozzle lip and generate new surface as the inner layer slides past a fractured outer layer.[64] In contrast, the instabilities in this work form past the nozzle exit, where the filament reaches its deepest extent into the bath (Figure S29). It is possible that sharkskin instabilities do not emerge in this study because flow rates are too slow or because sharkskin instabilities are linked

https://doi.org/10.1021/acsami.2c08047
ACS Appl. Mater. Interfaces XXXX, XXX, XXX−XXX

to polymer stretch and entanglements,[64] while the fluids studied here are colloidal gels and low molecular weight resins. Another documented source of surface roughness in printed beams is buckling, as predicted by Euler–Bernoulli beam theory for elastic solids.[32,35] Beam theory predicts that the wavelength of the buckling instabilities increases with increasing ink modulus divided by support modulus,[32,35] which matches the trend here, where filaments become smoother with increasing viscosity ratio. However, because the instabilities form on short time scales while both the ink and support should be yielded, we expect that this roughness is controlled by viscous dissipation rather than elastic stresses. Further, beam buckling must be driven by a compressive stress along the length of the filament, such as interfacial tension[32] or cell-imposed stresses,[35] but the water-based inks in this work have no known compressive stress along their length. Instabilities can also appear due to turbulence at large Reynolds numbers,[65] but the Reynolds numbers in this work range from 10^{-4} to 10^{-1}. Finally, surface roughness can occur on filaments when the supports are composed of microgels with particle sizes on the same order as the filament diameter.[31] In this work, the Laponite-based gels are composed of flakes with diameters on the order of tens of nanometers, and aggregates on the scale of hundreds of micrometers are not expected.[66] As such, these instabilities are most comparable to Saffman–Taylor instabilities. However, in microgels with larger particle sizes, roughness could emerge via a separate mechanism, the structure of the support.

Roughness may additionally be influenced by interaction with the nozzle. In Figure S29B, a fingering instability is able to grow longer and thinner via pinning at the downstream edge of the nozzle. It is possible that because the filament does not project deeply into the bath at low viscosity ratios, the filament is more likely to be pinned at the downstream corner of the nozzle, leading to more roughness at low viscosity ratios.

Gravity, Drag, Transients, and Creep Hinder Shape Fidelity. Gravity may influence the printing process in multiple ways. At high support Laponite concentrations, the crevasse behind the nozzle never closes after printing because the hydrostatic pressure is lower than the yield stress of the support (Figure 6D).[8] Additionally, toward the bath surface, filament breakup is more common, potentially because the lower hydrostatic pressure leads to delayed crevasse closure, exposing the ink to air. Because the air–ink interface has a higher interfacial tension and lower viscosity than the support–ink interface and thus lower *Ca*, this exposure makes Plateau–Rayleigh instabilities more likely. Density differences between the ink and support can also cause defects. At very low support viscosities, the mineral oil inks float to the top of the bath. On the other end, PEGDA-based inks sink in low-viscosity supports, for both vertical lines (Figure S30) and horizontal lines. Thus, if a low-viscosity support is necessary because the ink has a low viscosity, the support should also be density matched to the ink.

Viscous drag can cause leaking. By Stokes' law, the drag force on an object scales with the product of the viscosity of the matrix fluid and the translation speed.[67] Because of Stokes' drag, the downstream outer wall of the nozzle is at a low pressure for horizontal lines, and the nozzle exit is at a low pressure for vertical lines. These low pressures in horizontal lines were previously documented in simulations of embedded 3D printing.[29] A complementary simulation of a vertical filament is shown in Figure S19. As expected, the region just below the walls at the tip of the nozzle is at a lower pressure. The pressure differential between the inside of the nozzle and these drag-induced low-pressure regions drives fluid out of the nozzle. This pressure differential still exists when there is no imposed extrusion pressure, which is why the nozzle leaks at the end of vertical lines. The pressure differential between the inside and exit of the nozzle is the same for vertical and horizontal filaments (Figure S19). For horizontal filaments, the pressure continues to drop, farther into the bath and downstream of the nozzle, which would draw fluid away from the nozzle exit. For vertical filaments, the pressure reaches a minimum just outside the nozzle and, then, rises along the filament. This local minimum could lead to lower flow rates in vertical filaments. These pressure differentials may explain why there is a region in viscosity space where vertical lines contract, and horizontal lines are full length (Figure 6C,D), and there is a region in velocity space where vertical lines contract and horizontal lines rupture (Figure 6A,B).

Transients can lead to underflow and leaking. While mass flow controllers reach their target pressure faster than syringe pumps, they still have finite pressure transients. Viscous dissipation in the ink can also contribute to transients in flow rate. Startup transients are visible at fast support speeds, where the vertical filaments are shorter and widen toward the top, as the flow rate reaches its final value (Figure S18). Transients at the end of the line, where viscous dissipation allows the ink to continue flowing even after the driving pressure is removed, can also contribute to leaking.

Creep can also complicate flow rate calibration. The rheological behavior of Laponite in water depends strongly on its shear history.[66] During the calibration process, flow rates for a certain pressure can change over the course of multiple measurements. The vertical filaments in the water/Laponite viscosity sweep in Figure 7E may have been underextruded because the shear history of the ink shifted between calibration and printing. To avoid these shifts in calibration, it may be beneficial to use inks with a short recovery time and minimal creep.

Capillary Number Dominates Defects at Nonzero Surface Tension. At nonzero interfacial tension, $Ca = v_{\mathrm{ink}}\eta_{\mathrm{sup}}/\sigma$ strongly correlates with the cross-section aspect ratio, horizontal segment length, horizontal line length, vertical line length, vertical line diameter, and horizontal line roughness. Similarly, $\overline{d_{\mathrm{PR,sup}}} = (\tau_{\mathrm{y,sup}} d_{\mathrm{i}}/\sigma)\sqrt{v_{\mathrm{ink}}/v_{\mathrm{sup}}}$ strongly correlates with the same metrics. Both *Ca* and $\overline{d_{\mathrm{PR,sup}}}$ depend on similar variables: the ink speed and support rheology balanced against the interfacial tension. However, *Ca* uses the local viscosity and $\overline{d_{\mathrm{PR,sup}}}$ uses the yield stress.

Previous works have proposed that $\overline{d_{\mathrm{PR,sup}}}$ and other yield stress-based parameters predict whether a filament breaks into droplets.[10,32] However, for most Herschel–Bulkley fluids, the yield stress correlates with the local viscosity, leading to difficulty separating viscous effects from elastic effects. This work suggests that viscous dissipation may be equally or more important than yielding. From a practical standpoint, the distinction does not matter. Regardless of the physics of the process, suppressing droplets via support rheology, e.g., by adding more rheological modifier to the bath, will usually increase both the yield stress and local viscosity of the bath. Only an experiment that truly isolates the local viscosities from the yield stresses can prove which factor is more important.

https://doi.org/10.1021/acsami.2c08047
ACS Appl. Mater. Interfaces XXXX, XXX, XXX−XXX

This work shows several pieces of evidence that the critical diameter construction is inadequate at short time scales and that both yielding and viscous dissipation may be necessary to characterize the system. First, there is neither a critical $\overline{d_{\mathrm{PR,sup}}}$ nor a critical Ca where filaments break up into droplets (Figure S14). Second, in many cases, Ca better unifies the trends in viscosity and speed sweeps. Third, at nonzero interfacial tension, filament cross-sectional shapes and sizes are nearly the same just after deposition and 4 min after deposition (Figure S10B,C,D). Because almost all of the shape evolution is finished just after deposition, the shape evolution occurs while the ink and support are both yielded. Fourth, filaments often rupture into droplets directly at the nozzle tip, where the support is yielded (Figure S11A). Alternatively, they cling to the nozzle during printing, as shown in Figure S24A and previous simulations.[29] If the interfacial tension only needed to overcome yielding, not just viscous dissipation, the filaments would come out as full filaments and, then, rupture into droplets long after printing. Because these droplets form as they are leaving the nozzle, they form within the yielded zone, which was documented in simulations[29] and particle imaging velocimetry experiments.[39] At low support Laponite concentrations and high ink silica concentrations, a continuous filament is initially extruded and then the filament later breaks into droplets (Figure S11B). In this case, the viscous dissipation delays rupture, but because the interfacial tension is high enough to yield the support, rupture eventually occurs. As such, both viscous dissipation and yielding control the printed morphology.

The formulation of Ca that best unifies the trends in viscosity sweeps and speed sweeps uses the viscosity of the support and the velocity of the ink. As with all works, this formulation is tailored to the specific geometry of this system. Others have used different formulations. For example, in microfluidic t-channels, behaviors can be mapped across a two-dimensional space formed by the injected capillary number and continuous capillary number.[68] However, the change in direction that takes place in the printing of horizontal lines makes the relationship between the ink speed and support viscosity important. More closely relevant, the diameter of droplets in embedded droplet printing has previously been shown to scale inversely with the formulation we refer to as the support capillary number, which uses the translation speed and local support viscosity.[5] In this work, the support viscosity scales inversely with the translation speed, so the support capillary number fails to capture variations in droplet size with print speeds (Figure S13). Moreover, because the probed support viscosity space is mostly focused on the transition from filaments to droplets and measurements are collected soon after printing, this work describes few spherical droplets. Rather than transitioning to smaller spherical droplets with increasing support viscosity, this work demonstrates thinner, longer droplets with increasing support viscosity. The previous work showed that increasing the flow speed shifts the curve toward larger droplets,[5] which is consistent with the increase in droplet size shown in Figure 6B and the increase in droplet length with increasing Ca in Figure 7A.

At low Ca and $\overline{d_{\mathrm{PR,sup}}}$, we expect capillarity-induced rupture and contraction.[37,38,43] This is consistent with the experiments in this work. Decreasing the capillary number causes filaments to become rounder, smoother, shorter, and thicker. In other words, they become more spherical. As such, nonzero interfacial tensions present trade-offs in filament quality. One could produce rounder and smoother filaments by increasing the interfacial tension, decreasing the ink speed, or decreasing the support viscosity, but the filaments may become short and thick, potentially harming shape fidelity and resolution. The filament aspect ratio is close to 1 at a capillary number of 10^{-1}, but at the same capillary number, the programmed length is 20% of the intended length. However, if Ca is high enough to suppress contraction, a nonzero interfacial tension system could still be justifiable, given improvements in roughness and aspect ratio compared to zero interfacial tension fluids at the same viscosity ratio.

The viscosity ratio is correlated with many metrics at nonzero interfacial tension. It is not a coincidence that the viscosity ratio correlates with the cross-section aspect ratio, horizontal droplet length, horizontal line length, vertical line length, and vertical line diameter, but with weaker correlation strengths than the capillary number and normalized critical diameter. The support rheology is present in all three parameters. Moreover, in many nonzero interfacial tension correlation tables, the viscosity ratio correlation has strength similar to that of the support viscosity and the correlation with the ink viscosity is much weaker. As such, for both miscible and immiscible material systems, the most influential design choice is the rheology of the support. Because the support rheology has such a strong influence, it is important that the support properties do not change over time.

CONCLUSION

In this work, we used model materials to investigate the effect of ink and support rheology, interfacial tension, and print speeds on the morphology of individual vertical and horizontal filaments in embedded 3D printing. From these experiments, we make the following recommendations.

If the ink and support must be miscible, ensure that the local ink viscosity is slightly greater than the local support viscosity near the nozzle. This can be achieved via the concentration of rheological modifiers in the ink and support, or by choosing flow speeds and translation speeds that shift the local viscosities via shear thinning. By keeping the local viscosity ratio slightly above 1, filaments will be round and smooth. If viscosity ratios are lower, filaments take on a fin-shaped cross-section, with a tall aspect ratio and sharp edge at the top. Filaments at low viscosity ratios are also vulnerable to Saffman−Taylor instabilities, which lead to surface roughness on individual filaments. Additionally, for miscible fluids, concentrations of mobile species should be similar between the ink and support, to suppress swelling.

If the ink and support can be immiscible, choose a nonzero interfacial tension to achieve rounder, smoother filaments and suppress swelling. In order to prevent capillarity-induced shrinkage and rupture of printed filaments, $Ca = v_{\mathrm{ink}}\eta_{\mathrm{sup}}/\sigma$ must be high. As a trade-off, a high Ca will produce a noncircular cross-section, although it will be rounder and smoother than the cross-section achieved at zero interfacial tension with an equivalent viscosity ratio. A high Ca can be achieved by modifying the ink flow rate, the support composition, or the translation speed, or by lowering the interfacial tension via surfactants[69] or particle stabilizers.[57]

Further work is necessary to more precisely understand the physics of this printing process. This work shows that viscous dissipation is likely more important than yielding, and the short-term morphology of filaments is determined within the yielded zone around the nozzle. However, for the fluids in this work, local viscosities were correlated with yield stresses. Experiments or simulations which isolate the yield stress from the local viscosity would help to elucidate the underlying physics. These experiments indicated that density contrast and nozzle wetting might have an effect on the vertical position of the filament within the bath. Future work could isolate these variables explicitly in the experimental design. These experiments were also conducted on materials which were never cured. Curing methods which begin immediately after contact with the bath, such as ionic curing of alginate, may change the structure evolution of filaments. Further work could control for solidification timing. Leaking may be more prevalent in embedded 3D printing than DIW, because, in addition to transients, viscous drag produces pressure gradients that pull ink out of the nozzle even without a driving flow pressure. Negative pressures may be necessary to prevent leaking. Finally, while we found that high viscosity ratios and capillary numbers suppress defects in individual filaments, they may also influence fusion between neighboring filaments,[28,40] corner defects,[39,60,70] cell survival,[33] curing,[60] and defects in full parts. Scaling up in geometry and complexity will be necessary to fully understand the physics of embedded 3D printing.

■ ASSOCIATED CONTENT

Supporting Information

The Supporting Information is available free of charge at https://pubs.acs.org/doi/10.1021/acsami.2c08047.

> Summary of scaling variable definitions; densities; rheologies of all inks and supports; comparison between experiments and simulations; Spearman rank correlation tables; correlation plots; images of printed lines; vertical shift (bottom-heaviness) data; printed lines' time evolutions, time series images; simulated pressure fields; vertical displacement data; (PDF)

■ AUTHOR INFORMATION

Corresponding Author

Leanne M. Friedrich − *Material Measurement Laboratory, National Institute of Standards and Technology, Gaithersburg, Maryland 20899, United States;* orcid.org/0000-0002-0382-3980; Email: Leanne.Friedrich@nist.gov

Authors

Ross T. Gunther − *Materials Science and Engineering, Georgia Institute of Technology, Atlanta, Georgia 30332, United States;* orcid.org/0000-0002-6442-5396

Jonathan E. Seppala − *Material Measurement Laboratory, National Institute of Standards and Technology, Gaithersburg, Maryland 20899, United States*

Complete contact information is available at: https://pubs.acs.org/10.1021/acsami.2c08047

Author Contributions

L.M.F.: Conceptualization, data curation, formal analysis, investigation, methodology, software, visualization, writing—original draft. R.T.G.: Software, writing—review and editing. J.E.S.: Resources, supervision, writing—review and editing.

Notes

The authors declare no competing financial interest.

■ ACKNOWLEDGMENTS

This work was supported by a National Research Council postdoctoral fellowship and a National Institute of Standards and Technology Summer Undergraduate Research Fellowship. Certain commercial equipment, instruments, or materials are identified in this paper in order to specify the experimental procedure adequately. Such identification is not intended to imply recommendation or endorsement by the National Institute of Standards and Technology, nor is it intended to imply that the materials or equipment identified are necessarily the best available for the purpose.

■ REFERENCES

(1) Zhou, L.-y.; Fu, J.; He, Y. A Review of 3D Printing Technologies for Soft Polymer Materials. *Adv. Funct. Mater.* **2020**, *30*, 2000187.

(2) O'Bryan, C. S.; Bhattacharjee, T.; Niemi, S. R.; Balachandar, S.; Baldwin, N.; Ellison, S. T.; Taylor, C. R.; Sawyer, W. G.; Angelini, T. E. Three-Dimensional Printing with Sacrificial Materials for Soft Matter Manufacturing. *MRS Bull.* **2017**, *42*, 571−577.

(3) McCormack, A.; Highley, C. B.; Leslie, N. R.; Melchels, F. P. 3D Printing in Suspension Baths: Keeping the Promises of Bioprinting Afloat. *Trends Biotechnol.* **2020**, *38*, 584−593.

(4) Shiwarski, D. J.; Hudson, A. R.; Tashman, J. W.; Feinberg, A. W. Emergence of FRESH 3D Printing as a Platform for Advanced Tissue Biofabrication. *APL Bioengineering* **2021**, *5*, 010904.

(5) Nelson, A. Z.; Kundukad, B.; Wong, W. K.; Khan, S. A.; Doyle, P. S. Embedded Droplet Printing in Yield-Stress Fluids. *Proc. Natl. Acad. Sci. U.S.A.* **2020**, *117*, 5671−5679.

(6) Kolesky, D. B.; Truby, R. L.; Gladman, A. S.; Busbee, T. A.; Homan, K. A.; Lewis, J. A. 3D Bioprinting of Vascularized, Heterogeneous Cell-Laden Tissue Constructs. *Adv. Mater.* **2014**, *26*, 3124−3130.

(7) Zhao, J.; Hussain, M.; Wang, M.; Li, Z.; He, N. Embedded 3D Printing of Multi-Internal Surfaces of Hydrogels. *Additive Manufacturing* **2020**, *32*, 101097.

(8) Bhattacharjee, T.; Zehnder, S. M.; Rowe, K. G.; Jain, S.; Nixon, R. M.; Sawyer, W. G.; Angelini, T. E. Writing in the Granular Gel Medium. *Sci. Adv.* **2015**, *1*, No. e1500655.

(9) Ayan, B.; Celik, N.; Zhang, Z.; Zhou, K.; Kim, M. H.; Banerjee, D.; Wu, Y.; Costanzo, F.; Ozbolat, I. T. Aspiration-assisted Freeform Bioprinting of Tissue Spheroids in a Yield-Stress Gel. *Commun. Phys.* **2020**, *3*, 183.

(10) Calais, T.; Sanandiya, N. D.; Jain, S.; Kanhere, E. V.; Kumar, S.; Yeow, R. C.-H.; Valdivia y Alvarado, P. Freeform Liquid 3D Printing of Soft Functional Components for Soft Robotics. *ACS Appl. Mater. Interfaces* **2022**, *14*, 2301−2315.

(11) Jin, Y.; Song, K.; Gellermann, N.; Huang, Y. Printing of Hydrophobic Materials in Fumed Silica Nanoparticle Suspension. *ACS Appl. Mater. Interfaces* **2019**, *11*, 29207−29217.

(12) Sakai, S.; Harada, R.; Kotani, T. Freeform 3D Bioprinting Involving Ink Gelation by Cascade Reaction of Oxidase and Peroxidase: A Feasibility Study Using Hyaluronic Acid-Based Ink. *Biomolecules* **2021**, *11*, 1908.

(13) Hinton, T. J.; Jallerat, Q.; Palchesko, R. N.; Park, J. H.; Grodzicki, M. S.; Shue, H.-J.; Ramadan, M. H.; Hudson, A. R.; Feinberg, A. W. Three-Dimensional Printing of Complex Biological Structures by Freeform Reversible Embedding of Suspended Hydrogels. *Scie. Adv.* **2015**, *1*, No. e1500758.

(14) Hinton, T. J.; Hudson, A.; Pusch, K.; Lee, A.; Feinberg, A. W. 3D Printing PDMS Elastomer in a Hydrophilic Support Bath via Freeform Reversible Embedding. *ACS Biomaterials Science and Engineering* **2016**, *2*, 1781−1786.

(15) Luo, G.; Yu, Y.; Yuan, Y.; Chen, X.; Liu, Z.; Kong, T. Freeform, Reconfigurable Embedded Printing of All-Aqueous 3D Architectures. *Adv. Mater.* **2019**, *31*, 1904631.

(16) Highley, C. B.; Rodell, C. B.; Burdick, J. A. Direct 3D Printing of Shear-Thinning Hydrogels into Self-Healing Hydrogels. *Adv. Mater.* **2015**, *27*, 5075−5079.

(17) Skylar-Scott, M. A.; Uzel, S. G. M.; Nam, L. L.; Ahrens, J. H.; Truby, R. L.; Damaraju, S.; Lewis, J. A. Biomanufacturing of Organ-Specific Tissues with High Cellular Density and Embedded Vascular Channels. *Sci. Adv.* **2019**, *5*, No. eaaw2459.

(18) Moxon, S. R.; Cooke, M. E.; Cox, S. C.; Snow, M.; Jeys, L.; Jones, S. W.; Smith, A. M.; Grover, L. M. Suspended Manufacture of Biological Structures. *Adv. Mater.* **2017**, *29*, 1605594.

(19) Senior, J. J.; Cooke, M. E.; Grover, L. M.; Smith, A. M. Fabrication of Complex Hydrogel Structures Using Suspended Layer Additive Manufacturing (SLAM). *Adv. Funct. Mater.* **2019**, *29*, 1904845.

(20) O'Bryan, C. S.; Bhattacharjee, T.; Marshall, S. L.; Sawyer, W. G.; Angelini, T. E. Commercially Available Microgels for 3D Bioprinting. *Bioprinting* **2018**, *11*, No. e00037.

(21) De Santis, M. M.; et al. Extracellular-Matrix-Reinforced Bioinks for 3D Bioprinting Human Tissue. *Adv. Mater.* **2021**, *33*, 2005476.

(22) Zhu, K.; Shin, S. R.; van Kempen, T.; Li, Y. C.; Ponraj, V.; Nasajpour, A.; Mandla, S.; Hu, N.; Liu, X.; Leijten, J.; Lin, Y. D.; Hussain, M. A.; Zhang, Y. S.; Tamayol, A.; Khademhosseini, A. Gold Nanocomposite Bioink for Printing 3D Cardiac Constructs. *Adv. Funct. Mater.* **2017**, *27*, 1605352.

(23) Shapira, A.; Noor, N.; Oved, H.; Dvir, T. Transparent Support Media for High Resolution 3D Printing of Volumetric Cell-Containing ECM Structures. *Biomedical Materials* **2020**, *15*, 045018.

(24) Noor, N.; Shapira, A.; Edri, R.; Gal, I.; Wertheim, L.; Dvir, T. 3D Printing of Personalized Thick and Perfusable Cardiac Patches and Hearts. *Advanced Science* **2019**, *6*, 1900344.

(25) Comminal, R.; Serdeczny, M. P.; Pedersen, D. B.; Spangenberg, J. Motion Planning and Numerical Simulation of Material Deposition at Corners in Extrusion Additive Manufacturing. *Additive Manufacturing* **2019**, *29*, 100753.

(26) Duty, C.; Ajinjeru, C.; Kishore, V.; Compton, B.; Hmeidat, N.; Chen, X.; Liu, P.; Hassen, A.; Lindahl, J.; Kunc, V. What Makes a Material Printable? A Viscoelastic Model for Extrusion-Based 3D Printing of Polymers. *Journal of Manufacturing Processes* **2018**, *35*, 526−537.

(27) Compaan, A. M.; Song, K.; Chai, W.; Huang, Y. Cross-Linkable Microgel Composite Matrix Bath for Embedded Bioprinting of Perfusable Tissue Constructs and Sculpting of Solid Objects. *ACS Appl. Mater. Interfaces* **2020**, *12*, 7855−7868.

(28) Ning, L.; Mehta, R.; Cao, C.; Theus, A.; Tomov, M.; Zhu, N.; Weeks, E. R.; Bauser-Heaton, H.; Serpooshan, V. Embedded 3D Bioprinting of Gelatin Methacryloyl-Based Constructs with Highly Tunable Structural Fidelity. *ACS Appl. Mater. Interfaces* **2020**, *12*, 44563−44577.

(29) Friedrich, L. M.; Seppala, J. E. Simulated Filament Shapes in Embedded 3D Printing. *Soft Matter* **2021**, *17*, 8027.

(30) Ding, H.; Chang, R. Printability Study of Bioprinted Tubular Structures Using Liquid Hydrogel Precursors in a Support Bath. *Applied Sciences* **2018**, *8*, 403.

(31) Jeon, O.; Lee, Y. B.; Jeong, H.; Lee, S. J.; Wells, D.; Alsberg, E. Individual Cell-only Bioink and Photocurable Supporting Medium for 3D Printing and Generation of Engineered Tissues with Complex Geometries. *Materials Horizons* **2019**, *6*, 1625−1631.

(32) O'Bryan, C. S.; Brady-Miné, A.; Tessmann, C. J.; Spotz, A. M.; Angelini, T. E. Capillary Forces Drive Buckling, Plastic Deformation, and Break-Up of 3D Printed Beams. *Soft Matter* **2021**, *17*, 3886−3894.

(33) Spencer, A. R.; Shirzaei Sani, E.; Soucy, J. R.; Corbet, C. C.; Primbetova, A.; Koppes, R. A.; Annabi, N. Bioprinting of a Cell-Laden Conductive Hydrogel Composite. *ACS Appl. Mater. Interfaces* **2019**, *11*, 30518−30533.

(34) Friedrich, L.; Begley, M. In situ Characterization of Low-Viscosity Direct Ink Writing: Stability, Wetting, and Rotational Flows. *J. Colloid Interface Sci.* **2018**, *529*, 599−609.

(35) Morley, C. D.; et al. Quantitative Characterization of 3D Bioprinted Structural Elements under Cell Generated Forces. *Nat. Commun.* **2019**, *10*, 3029.

(36) Style, R. W.; Jagota, A.; Hui, C. Y.; Dufresne, E. R. Elastocapillarity: Surface Tension and the Mechanics of Soft Solids. *Annual Review of Condensed Matter Physics* **2017**, *8*, 99−118.

(37) Powers, T. R.; Zhang, D.; Goldstein, R. E.; Stone, H. A. Propagation of a Topological Transition: The Rayleigh Instability. *Phys. Fluids* **1998**, *10*, 1052−1057.

(38) Stone, H. A.; Bentley, B. J.; Leal, L. G. An Experimental Study of Transient Effects in the Breakup of Viscous Drops. *J. Fluid Mech.* **1986**, *173*, 131−158.

(39) Grosskopf, A.; Truby, R.; Kim, H.; Perazzo, A.; Lewis, J. A.; Stone, H. A. Viscoplastic Matrix Materials for Embedded 3D Printing. *ACS Appl. Mater. Interfaces* **2018**, *10*, 23353−23361.

(40) Friedrich, L.; Begley, M. Changes in Filament Microstructures during Direct Ink Writing with Yield Stress Fluid Support. *ACS Applied Polymer Materials* **2020**, *2*, 2528−2540.

(41) Nirmalkar, N.; Chhabra, R. P.; Poole, R. J. On Creeping Flow of a Bingham Plastic Fluid past a Square Cylinder. *J. Non-Newtonian Fluid Mech.* **2012**, *171−172*, 17−30.

(42) Ouattara, Z.; Jay, P.; Blésès, D.; Magnin, A. Drag of a Cylinder Moving Near a Wall in a Yield Stress Fluid. *AIChE J.* **2018**, *64*, 4118−4130.

(43) Homma, S.; Koga, J.; Matsumoto, S.; Song, M.; Tryggvason, G. Breakup Mode of an Axisymmetric Liquid Jet Injected into Another Immiscible Liquid. *Chem. Eng. Sci.* **2006**, *61*, 3986−3996.

(44) Derby, B. Inkjet Printing of Functional and Structural Materials: Fluid Property Requirements, Feature Stability, and Resolution. *Annu. Rev. Mater. Res.* **2010**, *40*, 395−414.

(45) Friedrich, L. M.; Seppala, J. E. Suppression of Filament Defects in Embedded 3D Printing: Images and Videos of Single Filament Extrusion. *NIST Public Data Repository*; National Institute of Standards and Technology (NIST), 2022, *1.0.0*.

(46) Friedrich, L. M.; Seppala, J. E. Python Tools for Image analysis of embedded 3D printing. *NIST Public Data Repository*; National Institute of Standards and Technology (NIST), 2022, *1.0.0*.

(47) Thompson, A.; Taylor, B. N. *Guide for the Use of the International System of Units (SI)*, NIST Special Publication 811; National Institute of Standards and Technology (NIST), 2008.

(48) Friedrich, L. M.; Seppala, J. E. usnistgov/ShopbotPyQt. *Github*, 2021; https://github.com/usnistgov/ShopbotPyQt/releases/tag/v1.0.4.

(49) ThorLabs. *CAD models*. https://www.thorlabs.com/. Accessed July 24, 2020.

(50) Edmund Optics. *VZM 450 Zoom Imaging Lens CAD model*; https://www.edmundoptics.com/p/vzmtrade-450i-zoom-imaging-lens/11340/. Accessed July 24, 2020.

(51) Basler AG. *Basler ace acA800−510uc CAD model*; https://www.baslerweb.com/en/products/cameras/area-scan-cameras/ace/aca800-510uc/. Accessed July 24, 2020.

(52) Bradski, G. The OpenCV Library. *Dr. Dobb's Journal of Software Tools*; Miller Freeman, 2000; Vol. *25*, pp 120−123.

(53) Van Rossum, G.; Drake, F. L. *Python 3 Reference Manual*; CreateSpace: Scotts Valley, CA, USA, 2009.

(54) The OpenFOAM Foundation. *OpenFOAM*, ver. 8, 2020; https://openfoam.org/.

(55) Dinkgreve, M.; Paredes, J.; Denn, M. M.; Bonn, D. On Different Ways of Measuring "the" Yield Stress. *J. Non-Newtonian Fluid Mech.* **2016**, *238*, 233−241.

(56) Feng, W.; Chai, Y.; Forth, J.; Ashby, P. D.; Russell, T. P.; Helms, B. A. Harnessing Liquid-in-Liquid Printing and Micro-patterned Substrates to Fabricate 3-dimensional All-Liquid Fluidic Devices. *Nat. Commun.* **2019**, *10*, 1095.

(57) Xu, R.; Liu, T.; Sun, H.; Wang, B.; Shi, S.; Russell, T. P. Interfacial Assembly and Jamming of Polyelectrolyte Surfactants: A Simple Route To Print Liquids in Low-Viscosity Solution. *ACS Appl. Mater. Interfaces* **2020**, *12*, 18116−18122.

https://doi.org/10.1021/acsami.2c08047
ACS Appl. Mater. Interfaces XXXX, XXX, XXX−XXX

(58) Kovach, I.; Won, J.; Friberg, S. E.; Koetz, J. Completely Engulfed Olive/Silicone Oil Janus Emulsions with Gelatin and Chitosan. *Colloid Polym. Sci.* **2016**, *294*, 705−713.
(59) Prendergast, M. E.; Burdick, J. A. Computational Modeling and Experimental Characterization of Extrusion Printing into Suspension Baths. *Adv. Healthc. Mater.* **2022**, *11*, 2101679.
(60) Uchida, T.; Onoe, H. 4D Printing of Multi-Hydrogels Using Direct Ink Writing in a Supporting Viscous Liquid. *Micromachines* **2019**, *10*, 433.
(61) Saffman, P. G.; Taylor, G. I. The Penetration of a Fluid into a Porous Medium or Hele-Shaw Cell Containing a More Viscous Liquid. *Proc. R. Soc. London, Ser. A* **1958**, *245*, 312−329.
(62) Sherwood, J. D.; Nittmann, J. Gradient Governed Growth: the Effect of Viscosity Ratio on Stochastic Simulations of the Saffman-Taylor Instability. *Journal de physique Paris* **1986**, *47*, 15−22.
(63) McLean, J. W.; Saffman, P. The Effect of Surface Tension on the Shape of Fingers in a Hele Shaw Cell. *J. Fluid Mech.* **1981**, *102*, 455−469.
(64) Migler, K. B.; Son, Y.; Qiao, F.; Flynn, K. Extensional Deformation, Cohesive Failure, and Boundary Conditions during Sharkskin Melt Fracture. *J. Rheol.* **2002**, *46*, 383−400.
(65) Leblanc, K. J.; Niemi, S. R.; Bennett, A. I.; Harris, K. L.; Schulze, K. D.; Sawyer, W. G.; Taylor, C.; Angelini, T. E. Stability of High Speed 3D Printing in Liquid-Like Solids. *ACS Biomaterials Science and Engineering* **2016**, *2*, 1796−1799.
(66) Suman, K.; Joshi, Y. M. Microstructure and Soft Glassy Dynamics of an Aqueous Laponite Dispersion. *Langmuir* **2018**, *34*, 13079−13103.
(67) Stokes, G. G. On the Effect of Internal Friction of Fluids on the Motion of Pendulums. *Trans. Cambridge Philos. Soc.* **1851**, *9*, 8−106.
(68) Cubaud, T.; Mason, T. G. Capillary Threads and Viscous Droplets in Square Microchannels. *Phys. Fluids* **2008**, *20*, 053302.
(69) Posocco, P.; Perazzo, A.; Preziosi, V.; Laurini, E.; Pricl, S.; Guido, S. Interfacial Tension of Oil/Water Emulsions with Mixed Non-Ionic Surfactants: Comparison between Experiments and Molecular Simulations. *RSC Adv.* **2016**, *6*, 4723−4729.
(70) Friedrich, L.; Begley, M. Corner Accuracy in Direct Ink Writing with Support Material. *Bioprinting* **2020**, *19*, No. e00086.

https://doi.org/10.1021/acsami.2c08047
ACS Appl. Mater. Interfaces XXXX, XXX, XXX−XXX